Journal of Computational Physics 489 (2023) 112273

Contents lists available at ScienceDirect

Journal of Computational Physics

journal homepage: www.elsevier.com/locate/jcp

A family of well-balanced WENO and TENO schemes for atmospheric flows

Adrián Navas-Montilla *, Isabel Echeverribar

Fluid Dynamics Technologies, I3A-University of Zaragoza, Spain

ARTICLE INFO

Article history:
Received 6 December 2022
Received in revised form 25 April 2023
Accepted 1 June 2023
Available online 7 June 2023

Keywords:
Numerical weather prediction
Well-balanced
Very high order
Finite volumes
Turbulence

ABSTRACT

We herein present a novel methodology to construct very high order well-balanced schemes for the computation of the Euler equations with gravitational source term, with application to numerical weather prediction (NWP). The proposed method is based on augmented Riemann solvers, which allow preserving the exact equilibrium between fluxes and source terms at cell interfaces. In particular, the augmented HLL solver (HLLS) is considered. Different spatial reconstruction methods can be used to ensure a high order of accuracy in space (e.g. WENO, TENO, linear reconstruction), being the TENO reconstruction the preferred method in this work. To the knowledge of the authors, the TENO method has not been applied to NWP before, although it has been extensively used by the computational fluid dynamics community in recent years. Therefore, we offer a thorough assessment of the TENO method to evidence its suitability for NWP considering some benchmark cases which involve inertia and gravity waves as well as convective processes. The TENO method offers an enhanced behavior when dealing with turbulent flows and underresolved solutions, where the traditional WENO scheme proves to be more diffusive. The proposed methodology, based on the HLLS solver in combination with a very high-order discretization, allows carrying out the simulation of meso- and micro-scale atmospheric flows in an implicit Large Eddy Simulation manner. Due to the HLLS solver, the isothermal, adiabatic and constant Brunt-Väisälä frequency hydrostatic equilibrium states are preserved with machine accuracy.

1. Introduction

Operational and research Numerical Weather Prediction (NWP) dynamical cores have experimented an important transition in the last decade towards non-hydrostatic models. At the same time, the use of very high-order numerical schemes has become more popular, as they prove very efficient in modern HPC computing facilities and allow achieving a high resolution in space and time [32]. This allows adopting Large Eddy Simulation (LES) frameworks and enables the construction of Cloud Resolving Models, obtaining unprecedented resolution levels.

To construct a non-hydrostatic atmospheric model, the Navier-Stokes equations or their inviscid counterpart (i.e. the compressible Euler equations) are considered. In this work we will focus on the latter, being the Euler equations a suitable model for meso- and micro-scale phenomena [19,18,32]. We can find in the literature various formulations of the Euler equations for the construction of operational and research NWP dynamical cores. The most common version of the Euler

* Corresponding author.
E-mail address: anavas@unizar.es (A. Navas-Montilla).

https://doi.org/10.1016/j.jcp.2023.112273

equations for the NWP community is given by the equation for the conservation of mass, momentum and potential temperature [41]. The latter equation is derived from the equation for the conservation of energy when considering that the flow is adiabatic. Directly working with the potential temperature avoids additional computation steps when using moist sub-grid scale physical parameterizations, thus motivating the use of this version of the Euler equations [19].

Other possibility, which we will herein explore, is to use the original Euler equations, composed by the equations for the conservation of mass, momentum and energy. As outlined in [19], this equation set offers several advantages over the version of the Euler equations mentioned before. On the one hand, it is physically consistent both in the inviscid and in the viscous regimes, therefore it is possible to specify the actual viscous stresses if needed [18,19]. In addition, it directly represents the conservation of mass, momentum and energy and therefore such quantities can be conserved with machine accuracy provided the use of a suitable discretization [18]. Furthermore, since this equation set has been traditionally used by the Computational Fluid Dynamics (CFD) community, many of the numerical advances developed in this field can be easily adapted for NWP (e.g. spatial reconstruction schemes, Riemann solvers, etc.) [19,18].

Recently, very high-order spectral element (SE), discontinuous Galerkin (DG) and finite volume (FV) schemes have gained attention for NWP due to their high resolution and computational efficiency [33,19,42,23,18,30,31]. Atmospheric meso- and micro-scale flows are sometimes characterized by the presence of sharp gradients and turbulence, for which high-order FV schemes based on non-oscillatory reconstructions and total variation diminishing (TVD) approaches are very well suited. A very common choice is the essentially non-oscillatory (ENO) and weighted essentially non-oscillatory (WENO) schemes [27], which are based on a selective stencil selection procedure that ensures a high order of accuracy and are able to capture discontinuities without Gibbs oscillations. Since their introduction, a collection of improved WENO schemes have been designed in an attempt to achieve better spectral properties and avoid sub-optimal behavior at critical points [1,24,16, 64,59,58]. WENO methods have been extensively applied to a large variety of flows by the CFD community [5,56,50,51], as well as in the field of NWP [44,18,43,42,30,45,34,61].

A novel family of targeted essentially non-oscillatory (TENO) methods has been recently introduced for the computation of compressible flows [14]. The TENO method features an incremental stencil selection in an ENO-like manner, where one candidate stencil is either selected for the final reconstruction with the optimal weight, or discarded completely when discontinuities are present. According to [14,12], the TENO reconstruction ensures that the spectral properties are recovered exactly up to intermediate wavenumber range, delivering a better performance than the WENO method. In particular, this method proves very beneficial when considering the combination of sharp gradients of the flow variables and turbulence, which may be the case for many atmospheric flows of interest. The reader is referred to [13] for a complete review of TENO methods.

Apart from the choice of a suitable high-order reconstruction method, other properties must be accounted for when designing a numerical scheme for the resolution of non-hydrostatic atmospheric flows. Most atmospheric phenomena of interest can be considered small perturbations over an equilibrium state [18,9]. In particular, the Euler equations with gravitational source term admit different hydrostatic equilibrium states (e.g. isothermal equilibrium, adiabatic equilibrium, etc.). In order to accurately capture the propagation of such perturbations, the numerical schemes must preserve the relevant equilibrium states with machine accuracy, otherwise spurious waves would appear in the solution. Those numerical schemes able to preserve the equilibrium states of relevance with machine accuracy are called well-balanced schemes [3,22]. There is an extensive work on the design of well-balanced schemes for hyperbolic systems of conservation laws with source terms, such as the shallow water equations [3,22,15,63,7,21] and the Euler equations under gravitation [28,8,18,63,9,10]. We can find different approaches to construct high-order well-balanced schemes. One alternative is to design Riemann solvers so that they allow exactly balancing fluxes and source terms and preserve the Rankine-Hugoniot (RH) condition at cell interfaces with machine accuracy. These are called augmented Riemann solvers, and have been extensively used for the shallow water equations [29,35,39] and hemodynamic flows [36], but their application to atmospheric flows is scarce.

In this work, we explore the use of augmented Riemann solvers for the design of very high-order well-balanced schemes for the Euler equations with gravitational source term. We present a novel approach to construct a family of very high-order essentially non-oscillatory schemes, which can consider different spatial reconstruction methods (e.g. WENO, TENO and linear reconstructions) and different augmented Riemann solvers. The motivation for the use of augmented solvers is next outlined. The high-order piecewise reconstruction of variables leads to bi-valued pressures at cell interfaces, which produces an imbalance of the solution. To enforce the equilibrium, an artificial source term must be introduced in the definition of the Riemann Problem (RP). This artificial source may account for the thrust and energy associated to the pressure jump across the interface, which has a numerical origin, and leads to a non-homogeneous RP. To compute the solution of non-homogeneous RPs, augmented Riemann solvers are required. In this work, we will focus on the augmented HLL solver, referred to as HLLS solver [37], which is derived here for the first time for the Euler equations with gravity. This solver is able to preserve the RH condition at cell interfaces by considering an extra term in the definition of the numerical fluxes. To satisfy the exact equilibrium in the numerical solution, apart from the use of augmented solvers, a correction of the volume integral of the source term inside cells has to be considered. This correction is only computed at the beginning of the simulation using the equilibrium data. If we wanted to avoid the use of augmented solvers, another possibility would be to work with perturbation variables (i.e. by subtracting the equilibrium state). Nevertheless, our motivation is to show the definition and use of the HLLS solver for this set of equations since it cannot be found in previous literature and moreover, these ideas can be further extended to other applications (compressible flow in ducts with varying cross sectional area, atmospheric flows with source terms of a more complex nature, etc.).

Another novelty of this work is the application of the TENO method to NWP. We believe the benefits offered by such a reconstruction method make it a suitable candidate for the resolution of atmospheric flows. Therefore, we present a thorough assessment of the performance of the TENO scheme, in comparison with the traditional WENO and linear reconstructions, for the resolution of different phenomena involving the propagation of waves, discontinuous solutions and turbulent fields. Numerical results for 8 different test cases, involving 1D, 2D and 3D flows, are presented.

2. The mathematical model

We are interested in meso- and micro-scale atmospheric flows, which can be represented by the Euler equations with a gravitational source term and neglecting Coriolis forces [18]. We consider the original Euler equation set, written in terms of mass, momentum and total energy as follows

$$\frac{\partial \mathbf{U}}{\partial t}+\frac{\partial \mathbf{F}(\mathbf{U})}{\partial x}+\frac{\partial \mathbf{G}(\mathbf{U})}{\partial y}+\frac{\partial \mathbf{H}(\mathbf{U})}{\partial z}=\mathbf{S}, \tag{1}$$

with

$$\mathbf{U}=\begin{pmatrix}\rho\\ \rho u\\ \rho v\\ \rho w\\ E\end{pmatrix},\quad \mathbf{F}=\begin{pmatrix}\rho u\\ \rho u^2+p\\ \rho uv\\ \rho uw\\ u(E+p)\end{pmatrix},\quad \mathbf{G}=\begin{pmatrix}\rho v\\ \rho vu\\ \rho v^2+p\\ \rho vw\\ v(E+p)\end{pmatrix},\quad \mathbf{H}=\begin{pmatrix}\rho w\\ \rho wu\\ \rho wv\\ \rho w^2+p\\ w(E+p)\end{pmatrix},\quad \mathbf{S}=\begin{pmatrix}0\\ 0\\ 0\\ -\rho g\\ -\rho wg\end{pmatrix}, \tag{2}$$

where ρ is the density, ρu, ρv, ρw are the unit discharges in the x, y and z directions, p is the pressure and E is the total energy, which is expressed as

$$E=\rho\left(\frac{1}{2}\mathbf{v}^2+e\right), \tag{3}$$

with $\mathbf{v}^2=u^2+v^2+w^2$ the squared velocity and e the internal energy. The ideal gas relation is used as closure equation

$$p=\rho RT\,, \tag{4}$$

where R is the universal gas constant and T is the temperature. Using the relations $e=c_vT$ and $R=c_p-c_v$, one can write:

$$p=(\gamma-1)\left(E-\frac{1}{2}\rho\mathbf{v}^2\right), \tag{5}$$

with $\gamma=c_p/c_v$, where c_p and c_v are the specific heats at constant pressure and volume, respectively. Two additional variables of interest in atmospheric flows are the Exner pressure π and the potential temperature θ, defined as

$$\pi=\left(\frac{p}{p_0}\right)^{\frac{\gamma-1}{\gamma}},\quad \theta=\frac{T}{\pi}, \tag{6}$$

where p_0 is the reference pressure at $z=0$, modelled as $p=\rho_0RT_0$.

The Euler equations in (1) admit a hydrostatic equilibrium state with zero velocity in the z direction, which is given by [18]

$$w=0\,,\quad \frac{\partial p}{\partial z}=-\rho g\quad\Leftrightarrow\quad \frac{\gamma R}{\gamma-1}\theta\frac{\partial \pi}{\partial z}=-g. \tag{7}$$

The equilibrium states satisfying (7) will be denoted by $p=p^e(z)$ and $\rho=\rho^e(z)$ and will be considered only functions of z in this work. Different hydrostatic equilibrium conditions are encountered in practical atmospheric applications [18,31]:

- Isothermal equilibrium: When the temperature of the atmosphere is considered constant in the whole domain, we obtain the following equilibrium state

$$\rho^e=\rho_0\exp\left(-\frac{z}{RT_0}\right),\quad p^e=\rho^eRT_0=p_0\exp\left(-\frac{z}{RT_0}\right),\quad w^e=0\,. \tag{8}$$

  The velocity components u^e and v^e can take any arbitrary constant value.
- Adiabatic equilibrium: In the case of an adiabatic atmosphere, the equilibrium state reads

$$p^e=p_0\left(1-\frac{(\gamma-1)g}{\gamma R\theta_0}z\right)^{\frac{\gamma}{\gamma-1}},\quad \rho^e=\frac{p}{R\pi\theta}=\frac{p_0}{R\theta_0}\left(1-\frac{(\gamma-1)g}{\gamma R\theta_0}z\right)^{\frac{1}{\gamma-1}},\quad w^e=0\,, \tag{9}$$

  where θ is assumed constant and equal to the temperature at $z=0$, i.e. $\theta_0=T_0\equiv T(z=0)$. The velocity components u^e and v^e can take any arbitrary constant value.

- Equilibrium specified by a constant Brunt-Väisälä frequency, $\mathcal{N}$: In this case, the equilibrium state reads

$$p^e = p_0(\pi^e)^{\frac{\gamma}{\gamma-1}}, \quad \rho^e = \frac{p_0}{R\theta^e}(\pi^e)^{\frac{1}{\gamma-1}}, \quad w^e = 0, \tag{10}$$

where the equilibrium Exner pressure is given by

$$\pi^e = 1 + \frac{(\gamma-1)g^2}{\gamma R T_0 \mathcal{N}^2}\left(\exp\left(-\frac{\mathcal{N}^2}{g}z\right) - 1\right) \tag{11}$$

and the potential temperature is given by

$$\theta^e = T_0 \exp\left(\frac{\mathcal{N}^2}{g}z\right). \tag{12}$$

The velocity components u^e and v^e can take any arbitrary constant value.

A Jacobian matrix can be defined for each of the flux functions to construct

$$\mathcal{J}(\mathbf{U},\mathbf{n}) = \frac{\partial \mathbf{F}}{\partial \mathbf{U}}n_x + \frac{\partial \mathbf{G}}{\partial \mathbf{U}}n_y + \frac{\partial \mathbf{H}}{\partial \mathbf{U}}n_z, \tag{13}$$

where $\mathbf{n} = (n_x, n_y, n_z)$. The system in Equation (1) is said to be hyperbolic since $\mathcal{J}(\mathbf{U},\mathbf{n})$ in Equation (13) is diagonalizable with real eigenvalues for all $\mathbf{n} \in \mathbb{R}^3$ and for all $\mathbf{U} \in C$ with $C \subseteq \mathbb{R}^5$ the subset of physically relevant values of $\mathbf{U}$ [20].

The Euler system in Equation (1) satisfies the rotational invariance property, i.e. the projection of the flux in any arbitrary direction given by $\mathbf{n} = (n_x, n_y, n_z)$ can be expressed as

$$\mathbf{F}n_x + \mathbf{G}n_y + \mathbf{H}n_z = \mathbf{R}^{-1}\mathbf{F}(\mathbf{R}\mathbf{U}), \tag{14}$$

where $\mathbf{R}$ is a rotation matrix [55]

$$\mathbf{R} = \begin{pmatrix} 1 & 0 & 0 & 0 & 0 \\ 0 & \cos\alpha^{(y)}\cos\alpha^{(z)} & \cos\alpha^{(y)}\sin\alpha^{(z)} & \sin\alpha^{(y)} & 0 \\ 0 & -\sin\alpha^{(z)} & \cos\alpha^{(z)} & 0 & 0 \\ 0 & -\sin\alpha^{(y)}\cos\alpha^{(z)} & -\sin\alpha^{(y)}\sin\alpha^{(z)} & \cos\alpha^{(y)} & 0 \end{pmatrix} \tag{15}$$

and

$$n_x = \cos\alpha^{(y)}\cos\alpha^{(z)} \quad n_y = \cos\alpha^{(y)}\sin\alpha^{(z)} \quad n_z = \sin\alpha^{(y)}, \tag{16}$$

with $\alpha^{(y)}$ and $\alpha^{(z)}$ the angles of rotation around the y and z axis, respectively.

The knowledge of the eigenstructure of the Jacobian matrices of the Euler system in Equation (1) is required for the design of numerical schemes based on Riemann solvers. Thanks to the rotational invariance property, we will only need to examine the Jacobian matrix of the flux in one spatial direction. We choose the flux in the x direction for the sake of simplicity. The following Jacobian matrix is obtained [55]

$$\mathbf{J} = \frac{\partial \mathbf{F}}{\partial \mathbf{U}} = \begin{pmatrix} 0 & 1 & 0 & 0 & 0 \\ H\hat{\gamma} - a^2 - u^2 & u(3-\gamma) & -\hat{\gamma}v & -\hat{\gamma}w & \hat{\gamma} \\ -uv & v & u & 0 & 0 \\ -uw & w & 0 & u & 0 \\ \frac{1}{2}u\left(\hat{\gamma}\mathbf{v}^2 - H\right) & H - \hat{\gamma}u^2 & -\hat{\gamma}uv & -\hat{\gamma}uw & \gamma u \end{pmatrix}, \tag{17}$$

where $H = \frac{E+p}{\rho}$ is the total specific enthalpy, $a = \sqrt{\gamma p/\rho}$ is the wave celerity and $\hat{\gamma} = \gamma - 1$. The corresponding eigenvalues are

$$\lambda_1 = u - a, \quad \lambda_2 = \lambda_3 = \lambda_4 = u, \quad \lambda_5 = u + a \tag{18}$$

and the matrix of corresponding right eigenvectors (in columns) is [55]

$$\mathbf{P} = \begin{pmatrix} 1 & 1 & 0 & 0 & 1 \\ -a+u & u & 0 & 0 & a+u \\ v & v & 1 & 0 & v \\ w & w & 0 & 1 & w \\ H - au & \frac{1}{2}\mathbf{v}^2 & v & w & H + au \end{pmatrix}. \tag{19}$$

Such matrix allows to diagonalize the Jacobian as $\mathbf{\Lambda} = \mathbf{P}^{-1}\mathbf{J}\mathbf{P}$, where $\mathbf{\Lambda} = diag(\lambda_1, ..., \lambda_5)$ is a diagonal matrix.

3. Numerical model: well-balanced high-order FV scheme in Cartesian grid

Let us consider the Euler equations in (1)–(2) to compose the following Initial Boundary Value Problem (IBVP):

$$\begin{cases} \text{PDEs:} & \dfrac{\partial \mathbf{U}}{\partial t}+\dfrac{\partial \mathbf{F}}{\partial x}+\dfrac{\partial \mathbf{G}}{\partial y}+\dfrac{\partial \mathbf{H}}{\partial z}=\mathbf{S} \\ \text{IC:} & \mathbf{U}(\mathbf{x},0)=\mathring{\mathbf{U}}(\mathbf{x}) \quad \forall \mathbf{x}\in\Omega \\ \text{BC:} & \mathbf{U}(\mathbf{x},t)=\mathbf{U}_{\partial\Omega}(\mathbf{x},t) \quad \forall \mathbf{x}\in\partial\Omega \end{cases} \tag{20}$$

defined in the domain $\Omega\times[0,T]$, where $\Omega=[x_1,x_2]\times[y_1,y_2]\times[z_1,z_2]$ is the spatial domain. The initial condition is given by $\mathring{\mathbf{U}}(\mathbf{x})$ and the boundary condition by $\mathbf{U}_{\partial\Omega}(\mathbf{x},t)$. The spatial domain is discretized in $N_x\times N_y\times N_z$ volume cells, defined as

$$\Omega_{ijk}=\left[x_{i-\frac{1}{2}},x_{i+\frac{1}{2}}\right]\times\left[y_{j-\frac{1}{2}},y_{j+\frac{1}{2}}\right]\times\left[z_{j-\frac{1}{2}},z_{j+\frac{1}{2}}\right], \qquad i=1,...,N_x,\ j=1,...,N_y,\ k=1,...,N_z\,. \tag{21}$$

We consider a Cartesian grid, therefore the grid spacing will be denoted by Δx, Δy and Δz in each of the Cartesian directions. Inside each cell, at time t^n, the conserved quantities are generally defined as cell averages as:

$$\mathbf{U}^n_{ijk}=\frac{1}{\Delta x\Delta y\Delta z}\int_{\Omega_{ijk}}\mathbf{U}(\mathbf{x},t^n)dV\,, \tag{22}$$

where $dV=dxdydz$. Using the finite volume approach, the semi-discrete form of Equation (1) is written as

$$\frac{\partial \mathbf{U}_{ijk}}{\partial t}=\mathcal{L}(\mathbf{U}_{ijk}), \tag{23}$$

where $\mathcal{L}(\mathbf{U}_{ijk})$ is the discrete operator representing the convective flux terms

$$\mathcal{L}(\mathbf{U}_{ijk})=-\frac{\mathbf{F}^-_{i+1/2,j,k}-\mathbf{F}^+_{i-1/2,j,k}}{\Delta x}-\frac{\mathbf{G}^-_{i,j+1/2,k}-\mathbf{G}^+_{i,j-1/2,k}}{\Delta y}-\frac{\mathbf{H}^-_{i,j,k+1/2}-\mathbf{H}^+_{i,j,k-1/2}}{\Delta z}+\bar{\mathbf{S}}_{ijk}\,, \tag{24}$$

where $\mathbf{F}^{\pm}_{i\mp1/2,j}$, $\mathbf{G}^{\pm}_{i,j\mp1/2}$ and $\mathbf{H}^{\pm}_{i,j\mp1/2}$ are the numerical fluxes at cell interfaces and

$$\bar{\mathbf{S}}_{ijk}\approx\frac{1}{\Delta x\Delta y\Delta z}\int_{\Omega_{ijk}}\mathbf{S}(\mathbf{U})\,dzdydx \tag{25}$$

is the approximation of the spatial integral of the source terms.

The Strong Stability Preserving Runge–Kutta 3 (SSPRK3) scheme [18,48] is used to compute the numerical approximation at time level $n+1$ as follows

$$\begin{aligned} \mathbf{U}^{(1)}_{ijk}&=\mathbf{U}^n_{ijk}+\Delta t\mathcal{L}(\mathbf{U}^n_{ijk}),\\ \mathbf{U}^{(2)}_{ijk}&=\tfrac{3}{4}\mathbf{U}^n_{ijk}+\tfrac{1}{4}\mathbf{U}^{(1)}_{ijk}+\tfrac{1}{4}\Delta t\mathcal{L}(\mathbf{U}^{(1)}_{ijk}),\\ \mathbf{U}^{n+1}_{ijk}&=\tfrac{1}{3}\mathbf{U}^n_{ijk}+\tfrac{2}{3}\mathbf{U}^{(2)}_{ijk}+\tfrac{2}{3}\Delta t\mathcal{L}(\mathbf{U}^{(2)}_{ijk}). \end{aligned} \tag{26}$$

The time step, Δt, is computed dynamically according to the CFL condition to preserve the stability of the numerical solution [11].

The numerical scheme in Equations (24)-(26) requires some additional considerations for the preservation of the well-balanced property. To maintain equilibrium at the discrete level, we need

$$\mathcal{L}(\mathbf{U}^n_{ijk})=0\,, \tag{27}$$

which is achieved by ensuring the two following requirements:

- R1: Under equilibrium, the numerical fluxes at cell interfaces must be equal to the physical fluxes. This will be achieved using augmented Riemann solvers, which will include within the numerical fluxes a compensation of the pressure discontinuity in the edges in the form of an artificial source term, $\bar{\mathbf{S}}_{i+1/2}$, that accounts for the thrust and power associated to this pressure jump.
- R2: Under equilibrium, the volume integral of the source term inside cells must exactly balance the physical flux differences along the cell interfaces. This will be achieved by means of a correction term for the integral of the source term inside the cell, $\bar{\mathbf{S}}_{ijk}$.

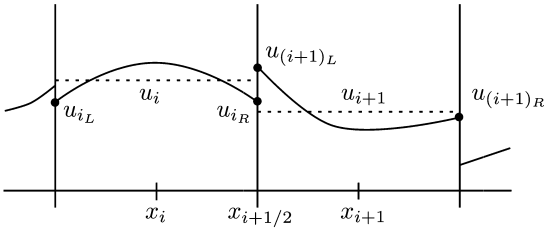

Fig. 1. Example of a 1D grid.

3.1. Spatial reconstructions of arbitrary order

The numerical fluxes at cell interfaces in Equation (24) are a function of a high-order reconstruction of the variables at each side of the interface. For example, the numerical flux in the x direction can be expressed as $\mathbf{F}^{\pm}_{i+1/2} = \mathbf{F}^{\pm}_{i+1/2}(\mathbf{U}_{i_R}, \mathbf{U}_{(i+1)_L})$, where $\mathbf{U}_{i_R}$ and $\mathbf{U}_{(i+1)_L}$ are the vectors of reconstructed conserved variables on the left and right hand sides of the interface. Note that the subscripts L, R refer to the cell and not to the interface. Vectors $\mathbf{U}_{i_R}$ and $\mathbf{U}_{(i+1)_L}$ are reconstructed in a component-wise manner, where a reconstruction procedure is applied to each component of the vector independently [48,18].

For the sake of simplicity, we will describe the reconstruction procedure for a scalar function $u(x)$, with cell averages u_i, which is defined along the x direction. The extension to 2 and 3 spatial dimensions is carried out by applying the procedure along each of the Cartesian directions [48,18]. In Fig. 1 we show the cell-averaged values and piecewise reconstructions of $u(x)$ inside two consecutive cells i and $i+1$. The reconstruction of $u(x)$ on the left and right hand side of the interface $x_{i+1/2}$ is denoted by u_{i_R} and $u_{(i+1)_L}$, respectively.

In this section, we describe two commonly used reconstruction methods: the traditional WENO reconstruction (also referred to as WENO-JS, after Jiang and Shu) and the TENO reconstruction. Both methods are used to build piecewise reconstructions inside each computational cell (Fig. 1), using information from neighboring cells. They can be defined for an arbitrary order of accuracy and are designed to recover the ENO property to capture discontinuities and to restore their linear counterparts when the solution is smooth. This feature is required for the meso-scale atmospheric problems herein considered, where sharp gradients (or even discontinuities) in the flow variables may be present, specially in the under-resolved cases.

The WENO method uses a variable set of stencils where lower order polynomials are first constructed. Then, these lower order polynomials are combined either to create a higher order polynomial in smooth regions or an off-center reconstruction able to capture discontinuities in non-smooth regions. The definition of a smoothness indicator permits to distinguish between those two cases. On the other hand, the TENO method features an incremental stencil selection in an ENO-like manner, where one candidate stencil is either selected for the final reconstruction with the optimal weight, or discarded completely when crossed by discontinuities. According to [14], the TENO reconstruction ensures that the spectral properties and the accuracy order of the underlying linear scheme can be recovered up to intermediate wavenumber range.

3.1.1. The WENO reconstruction

To carry out a reconstruction of degree $(2k-1)$ on the cell $\Omega_i = [x_{i-\frac{1}{2}}, x_{i+\frac{1}{2}}]$ for the function $u(x)$, k different stencils of k cells are needed. These stencils are given by $S_r(i) = \left\{\Omega_{i-r}, ..., \Omega_{i+k-r-1}\right\}$ $(r = 0, ..., k-1)$, where r represents the number of cells on the left hand side of Ω_i. These stencils can be combined to generate a bigger stencil $\mathcal{T}(i) = \cup_{r=0}^{k-1} S_r(i) = \left\{\Omega_{i-k+1}, ..., \Omega_{i+k-1}\right\}$.

The $(2k-1)$-th order WENO reconstructions of $u(x)$ on the left and right interfaces of an arbitrary i-th cell, i.e. at $x_{i-\frac{1}{2}}$ and $x_{i+\frac{1}{2}}$, are given by

$$u_{i_R} = \sum_{r=0}^{k-1} \omega_r u^{(r)}_{i_R}, \qquad u_{i_L} = \sum_{r=0}^{k-1} \omega_r u^{(r)}_{i_L} \tag{28}$$

where k is the number of candidate stencils, ω_r are the WENO nonlinear weights, yet to be defined, and $u^{(r)}_{i_R}$ and $u^{(r)}_{i_L}$ are the k-th order linear reconstructions in the candidate stencils, computed as a linear combination of cell averages as follows

$$u^{(r)}_{i_R} = \sum_{j=0}^{k-1} c^{(k)}_{rj} u_{i-r+j}, \qquad u^{(r)}_{i_L} = \sum_{j=0}^{k-1} \tilde{c}^{(k)}_{rj} u_{i-r+j}, \qquad r = 0, ..., k-1 \tag{29}$$

with $c^{(k)}_{rj}$ and $\tilde{c}^{(k)}_{rj}$ $c^{(k)}_{rj}$ coefficients derived from a Lagrange interpolation [27].

The nonlinear weights, ω_r, are computed as follows

$$\omega_r = \frac{\alpha_r}{\sum_{l=0}^{k-1} \alpha_l}, \qquad \alpha_r = \frac{d_r}{(\beta_r + \epsilon)^2}, \qquad r = 0, ..., k-1 \tag{30}$$

with $\epsilon = 10^{-6}$ a small constant to avoid division by zero, d_r the optimal weights and β_r the smoothness indicators proposed by Jiang and Shu in [27]. This method is also referred to as WENO-JS.

3.1.2. The TENO reconstruction

The $(2k-1)$-th order TENO reconstructions of $u(x)$ on the left and right interfaces of an arbitrary i-th cell, i.e. at $x_{i-\frac{1}{2}}$ and $x_{i+\frac{1}{2}}$, can be constructed using Equation (28) as done for the WENO scheme, considering a different definition of ω_r. The nonlinear weights are now computed as follows [14]

$$\omega_r = \frac{\alpha_r}{\sum_{l=0}^{k-1} \alpha_l}, \qquad \alpha_r = d_r \delta_r, \qquad r = 0, ..., k-1 \tag{31}$$

where α_r are computed using a ENO-like stencil selection methodology, with δ_r being the result of applying the following sharp cutoff function [12,14]

$$\delta_r = \begin{cases} 0 & \text{if } \chi_r < C_T \\ 1 & \text{otherwise} \end{cases}, \qquad r = 0, ..., k-1 \tag{32}$$

with χ_r a normalized smoothness measure and $C_T = 10^{-6}$ the threshold for the smoothness indicator that controls the participation of the candidate stencils [25,14]. This cutoff function ensures that a candidate stencil is fully suppressed for the final reconstruction if the measured smoothness is below a certain threshold, otherwise it is adopted with its original weight [14]. Note that an adaptive dissipation control (i.e. adaptive C_T) can be performed following the strategy in [12], but it is not considered here.

The coefficient χ_r is defined as the normalization of the smoothness measure, σ_r,

$$\chi_r = \frac{\sigma_r}{\sum_{l=0}^{k-1} \sigma_l}, \qquad \sigma_r = \frac{1}{(\beta_r + \epsilon)^6}, \qquad r = 0, ..., k-1. \tag{33}$$

Note that in this case, the smoothness measure is computed using the modified scale-separation formula proposed by Fu in [12], which is simpler than the original definition of σ_r [14] and leads to more efficient computations when increasing the order of accuracy. In Equation (33), we consider $\epsilon = 10^{-40}$ as indicated in [14,12].

3.2. Augmented solvers: the HLLS solver

The numerical fluxes are computed solving the Riemann problems at cell interfaces. Due to the piecewise nature of the spatial reconstruction (e.g. TENO), there will be a jump in the conserved variables and their fluxes across cell interfaces. To balance flux differences across cell interfaces and preserve the well-balanced property (i.e. the equilibrium of the discrete solution), we also consider the source term in the definition of the RP according to [40].

The RP in the x direction at the interface $i+1/2$, defined for the so-called x-split Euler equations, reads as:

$$\begin{cases} \dfrac{\partial \mathbf{W}}{\partial t} + \dfrac{\partial \mathbf{F}(\mathbf{W})}{\partial x} = \bar{\mathbf{S}}_{i+1/2} \\ \mathbf{W}(x,0) = \begin{cases} \mathbf{W}_{i_R} & x < 0 \\ \mathbf{W}_{(i+1)_L} & x > 0 \end{cases} \end{cases} \tag{34}$$

where $\mathbf{W}_{i_R}$ and $\mathbf{W}_{(i+1)_L}$ are the spatial reconstruction of the conserved variables on the left and right side of the cell interface, respectively, computed by means of the reconstruction method selected (e.g. WENO, TENO or linear reconstruction). Note that $\mathbf{W} = \mathbf{RU}$ is the vector of conserved variables rotated to the x-axis. From an implementation point of view, rotation operations can be simplified when considering Cartesian meshes, but we retain this notation for the sake of brevity. The term $\bar{\mathbf{S}}_{i+1/2}$ represents the approximation of the integral of the source term at cell interfaces. To preserve the discrete equilibrium, such term must balance the difference of fluxes at cell interfaces, according to the Rankine-Hugoniot (RH) condition

$$\mathbf{F}_{(i+1)_L} - \mathbf{F}_{i_R} = \bar{\mathbf{S}}_{i+1/2}\,. \tag{35}$$

The term $\bar{\mathbf{S}}_{i+1/2}$ is expressed as follows

$$\bar{\mathbf{S}}_{i+1/2} = \begin{pmatrix} 0 \\ \bar{s}^{(\rho u)}_{i+1/2} \\ 0 \\ 0 \\ \bar{s}^{(E)}_{i+1/2} \end{pmatrix}, \tag{36}$$

where $\bar{s}^{(\rho u)}_{i+1/2}$ and $\bar{s}^{(E)}_{i+1/2}$ are the approximation of the integral of the source terms in the momentum and energy equations, respectively, which must be designed to satisfy Eq. (35). Note that this is an artificial source term that must balance the thrust and power produced by the pressure jump across cell interfaces, which has a numerical origin (i.e. piecewise spatial reconstruction). The well-balanced property could also be satisfied if ommiting $\bar{s}^{(E)}_{i+1/2}$, but we have considered it for the sake of consistency in the derivation of the HLLS numerical fluxes.

For a RP for the Euler equations in (1), we can define an approximate Jacobian matrix of $\mathbf{F}$ that depends upon the left and right states, $\widetilde{\mathbf{J}}_{i+\frac{1}{2}} = \widetilde{\mathbf{J}}_{i+\frac{1}{2}}(\mathbf{W}_{i_R}, \mathbf{W}_{(i+1)_L})$, using Roe averages as follows [55]

$$\widetilde{\mathbf{J}}_{i+\frac{1}{2}} = \begin{pmatrix} 0 & 1 & 0 & 0 & 0 \\ \tilde{H}\hat{\gamma} - \tilde{a}^2 - \tilde{u}^2 & \tilde{u}(3-\gamma) & -\hat{\gamma}\tilde{v} & -\hat{\gamma}\tilde{w} & \hat{\gamma} \\ -\tilde{u}\tilde{v} & \tilde{v} & \tilde{u} & 0 & 0 \\ -\tilde{u}\tilde{w} & \tilde{w} & 0 & \tilde{u} & 0 \\ \frac{1}{2}\tilde{u}\left(\hat{\gamma}\tilde{\mathbf{v}}^2 - H\right) & \tilde{H} - \hat{\gamma}\tilde{u}^2 & -\hat{\gamma}\tilde{u}\tilde{v} & -\hat{\gamma}\tilde{u}\tilde{w} & \gamma\tilde{u} \end{pmatrix}_{i+\frac{1}{2}} \tag{37}$$

with the Roe averages denoted by $\tilde{(\cdot)}$ and defined in [55].

As mentioned above, a particular discretization of the source term is required to preserve the discrete equilibrium (i.e. the RH condition in Equation (35)). According to [31], we propose to use the following approximation of the integral of the source term for the momentum and energy equations

$$\bar{s}^{(\rho u)}_{i+1/2} = \frac{\rho_{(i+1)_L} + \rho_{i_R}}{\rho^e_{(i+1)_L} + \rho^e_{i_R}} \left(p^e_{(i+1)_L} - p^e_{i_R} \right), \tag{38}$$

$$\bar{s}^{(E)}_{i+1/2} = \tilde{u}\bar{s}^{(\rho u)}_{i+1/2}, \tag{39}$$

where $\rho^e_{(i+1)_L}$, $\rho^e_{i_R}$, $p^e_{(i+1)_L}$ and $p^e_{i_R}$ are the left and right interface values of the equilibrium density and pressure, computed at the beginning of the simulation. The spatial reconstruction is carried out for the conserved variables (ρ, ρu, ρv, ρw, E), therefore the equilibrium pressure must be computed from (5). For instance, the reconstruction of the pressure on the right side of cell i is computed as follows

$$p^e_{i_R} = (\gamma - 1)E^e_{i_R} - \frac{1}{2}\rho^e_{i_R}\left((u^e_{i_R})^2 + (v^e_{i_R})^2 + (w^e_{i_R})^2 \right), \tag{40}$$

with $u^e_{i_R} = (\rho u)^e_{i_R}/\rho^e_{i_R}$, and so on for the other components of the velocity.

Under equilibrium, $\rho = \rho^e$, $p = p^e$ and $\tilde{u} = 0$, thus the RH condition in Equation (35) is satisfied, leading to

$$\begin{pmatrix} 0 \\ p^e_{(i+1)_L} - p^e_{i_R} \\ 0 \\ 0 \\ 0 \end{pmatrix} = \begin{pmatrix} 0 \\ \bar{s}^{(\rho u)}_{i+1/2} \\ 0 \\ 0 \\ 0 \end{pmatrix} \tag{41}$$

evidencing that the approximation of the integral of the source term at cell interfaces exactly balances the jump in the pressure across the cell interface. Note that only jumps across the interface are accounted, as we consider the x-split Euler equations.

Augmented Riemann solvers include the contribution of the source term as an extra wave of zero velocity at the interface ($x = 0$), which originates a jump of the fluxes and conserved variables across the interface. The approximate solution, hereafter referred to as $\hat{\mathbf{W}}(x,t)$, is therefore composed by at least (depending on the number of waves) two different internal states in the so-called star region, separated by a contact discontinuity at $x = 0$ produced by the source term [37,35]. In the vicinity of $x = 0$, left and right states of the approximate solution will be hereafter denoted by $\mathbf{W}^-_{i_R}$ and $\mathbf{W}^+_{(i+1)_L}$ respectively, expressed as:

$$\mathbf{W}^-_{i_R} = \lim_{x\to 0^-} \hat{\mathbf{W}}(x,t) \qquad \mathbf{W}^+_{(i+1)_L} = \lim_{x\to 0^+} \hat{\mathbf{W}}(x,t)\,. \tag{42}$$

Analogously, an approximate flux function $\hat{\mathbf{F}}(x,t)$ can be also defined with a similar structure than $\hat{\mathbf{W}}(x,t)$. In this case, also intercell values for the fluxes can be defined at both sides of the t axis as:

$$\mathbf{F}^{-}_{i+1/2} = \lim_{x\to 0^-} \hat{\mathbf{F}}(x,t) \qquad \mathbf{F}^{+}_{i+1/2} = \lim_{x\to 0^+} \hat{\mathbf{F}}(x,t)\,. \tag{43}$$

Augmented Riemann solvers are designed to satisfy the following relation

$$\mathbf{F}^{+}_{i+1/2} - \mathbf{F}^{-}_{i+1/2} = \widetilde{\mathbf{J}}_{i+\frac{1}{2}} \left(\mathbf{W}^{+}_{(i+1)_L} - \mathbf{W}^{-}_{i_R} \right), \tag{44}$$

which can also be expressed as

$$\bar{\mathbf{S}}_{i+\frac{1}{2}} = \widetilde{\mathbf{J}}_{i+\frac{1}{2}} \left(\mathbf{W}^{+}_{(i+1)_L} - \mathbf{W}^{-}_{i_R} \right), \tag{45}$$

noticing that, under steady state conditions (i.e. $\mathbf{F}^{-}_{i+1/2} = \mathbf{F}_{(i+1)_L}$ and $\mathbf{F}^{+}_{i+1/2} = \mathbf{F}_{i_R}$), Equation (35) is recovered.

The RP in (34) will be computed by means of the HLLS solver [37,40]. This is an incomplete non-linear solver that approaches the wave structure of the system by a 2-wave structure. When using the HLLS solver, the numerical fluxes at cell interfaces are computed as follows:

$$\mathbf{F}^{-}_{i+1/2} = \begin{cases} \mathbf{F}_{i_R} & \text{if} \quad S_1 \geq 0 \\ \mathbf{F}^{-,HLLS}_{i_R} & \text{if} \quad S_1 \leq 0 \leq S_2 \\ \mathbf{F}_{(i+1)_L} - \bar{\mathbf{S}}_{i+\frac{1}{2}} & \text{if} \quad S_2 \leq 0 \end{cases}, \quad \mathbf{F}^{+}_{i+1/2} = \begin{cases} \mathbf{F}_{i_R} + \bar{\mathbf{S}}_{i+\frac{1}{2}} & \text{if} \quad S_1 \geq 0 \\ \mathbf{F}^{+,HLLS}_{(i+1)_L} & \text{if} \quad S_1 \leq 0 \leq S_2 \\ \mathbf{F}_{i_{(i+1)_L}} & \text{if} \quad S_2 \leq 0 \end{cases} \tag{46}$$

where the HLLS fluxes are given by

$$\mathbf{F}^{-,HLLS}_{i_R} = \frac{\left(S_2\mathbf{F}_{i_R} - S_1\mathbf{F}_{(i+1)_L}\right) + S_1S_2(\mathbf{W}_{(i+1)_L} - \mathbf{W}_{i_R}) + S_1\left(\bar{\mathbf{S}}_{i+\frac{1}{2}} - S_2\bar{\mathbf{B}}_{i+\frac{1}{2}}\right)}{S_2 - S_1}, \tag{47}$$

$$\mathbf{F}^{+,HLLS}_{(i+1)_L} = \frac{\left(S_2\mathbf{F}_{i_R} - S_1\mathbf{F}_{(i+1)_L}\right) + S_1S_2(\mathbf{W}_{(i+1)_L} - \mathbf{W}_{i_R}) + S_2\left(\bar{\mathbf{S}}_{i+\frac{1}{2}} - S_1\bar{\mathbf{B}}_{i+\frac{1}{2}}\right)}{S_2 - S_1}, \tag{48}$$

where $\bar{\mathbf{B}}_{i+\frac{1}{2}}$ is a matrix related to the source term, originally defined in [37] as follows

$$\bar{\mathbf{B}}_{i+\frac{1}{2}} \equiv \mathbf{W}^{+}_{(i+1)_L} - \mathbf{W}^{-}_{i_R} = \widetilde{\mathbf{J}}^{-1}_{i+\frac{1}{2}} \bar{\mathbf{S}}_{i+\frac{1}{2}} \tag{49}$$

and the wave celerities, S_1 and S_2, still to be defined. We can compute $\bar{\mathbf{B}}_{i+\frac{1}{2}}$ from Equation (49), leading to

$$\bar{\mathbf{B}}_{i+\frac{1}{2}} = -\frac{1}{\tilde{\lambda}_1\tilde{\lambda}_5} \begin{pmatrix} 1 \\ 0 \\ \tilde{v} \\ \tilde{w} \\ \tilde{H} - \tilde{u}^2; \end{pmatrix} \bar{s}_{i+1/2}. \tag{50}$$

From Equation (49) we notice that, under equilibrium, we must have

$$\mathbf{W}_{(i+1)_L} - \mathbf{W}_{i_R} = \bar{\mathbf{B}}_{i+\frac{1}{2}} \tag{51}$$

however, $\bar{\mathbf{B}}_{i+\frac{1}{2}}$ in Equation (50) does not ensure the equality in Equation (51) at the discrete level, being only valid for the continuous case (i.e. when $d\rho = dp/a^2$). To satisfy (51), vector $\bar{\mathbf{B}}_{i+\frac{1}{2}}$ is redefined as follows

$$\bar{\mathbf{B}}_{i+\frac{1}{2}} = -\frac{1}{\tilde{\lambda}_1\tilde{\lambda}_5} \begin{pmatrix} \varphi^\star \\ 0 \\ \varphi^\star\tilde{v} \\ \varphi^\star\tilde{w} \\ \tilde{H} - \tilde{u}^2 + \frac{1}{2}(\varphi^\star - 1)(\tilde{v}^2 + \tilde{w}^2) \end{pmatrix} \bar{s}_{i+1/2}\,, \tag{52}$$

where $\varphi^\star$ is a correction term defined as

$$\varphi^\star = \tilde{a}^2 \left(\frac{\delta\rho^e_{i+\frac{1}{2}}}{\delta p^e_{i+\frac{1}{2}} + \epsilon} \right), \tag{53}$$

with $\epsilon = 10^{-14}$ a sufficiently small constant to avoid division by zero when the pressure jump across the interface is nil. In the limit to the continuous case, this correction term $\varphi^\star$ would approach to 1.

The use of the expressions in Equations (38) and (52), in combination with the following choice for the wave celerities

$$S_1 = \tilde{\lambda_1}\,, \quad S_2 = \tilde{\lambda_5} \tag{54}$$

allows to satisfy the discrete RH conditions for the HLLS solver, making Equations (47) and (48) become

$$\mathbf{F}^{-,HLLS}_{i_R} = \mathbf{F}_{i_R}\,, \qquad \mathbf{F}^{+,HLLS}_{(i+1)_L} = \mathbf{F}_{(i+1)_L} \tag{55}$$

under equilibrium, thus satisfying the requirement R1 for the well-balancing of the scheme.

3.3. Correction of the integral of the source term

To ensure the well-balanced property, the integral of the source term in Equation (23) must exactly balance the physical flux differences at cell interfaces under equilibrium (requirement R2). However, an imbalance may appear because the spatial reconstruction method is not able to reconstruct with machine accuracy some equilibrium states (i.e. those cases where p^e and ρ^e are not given by smooth polynomial functions). Requirement R2 can be achieved by means of a correction term for the integral of the source term inside the cell. We propose to compute $\bar{\mathbf{S}}_{ijk}$ as follows

$$\bar{\mathbf{S}}^n_{ijk} = \begin{pmatrix} 0 \\ 0 \\ 0 \\ -g\rho^n_{ijk} + \varphi_k \\ -g(\rho w)^n_{ijk} \end{pmatrix}, \tag{56}$$

where φ_k is a correction term defined as

$$\varphi_k = \frac{1}{\Delta z}\left(p^e_{k_R} - p^e_{k_L}\right) + g\rho^e_k, \tag{57}$$

which only depends on the z direction and can be computed at the beginning of the simulation. Note that the dependence of φ_k upon i and j has been omitted for the sake of simplicity.

The correction term φ_k represents the imbalance in the discrete equilibrium solution. As pointed out by Botta [4], this imbalance can be regarded as the truncation error of the spatial discretization, that is $\varphi_k = \mathcal{O}(\Delta z^p)$, with p the order of the spatial reconstruction.

Note that the numerical scheme presented above is reduced to the 1-st order Godunov's method when no spatial reconstruction is considered (i.e. $\mathbf{U}_{i_R} = \mathbf{U}_{i_L} = \mathbf{U}_i$)) and the explicit Euler integration in time is used. This is beneficial in terms of the implementation of the scheme, as we can run the 1-st order version of the scheme without additional modifications.

4. Numerical results

In this section, we assess the performance of the proposed scheme using 8 different test cases involving 1D, 2D and 3D flows. For the TENO reconstruction, a threshold of $C_T = 10^{-6}$ is used following the recommendations from the literature, unless other value is specified.

4.1. Case 1. Well-balancing

This test case allows assessing the well-balancing of the schemes and has been used in previous studies [18,31,62]. We consider as initial condition the hydrostatic isothermal equilibrium in Equation (8) with

$$\rho_0 = 1\,, p_0 = 1\,, \quad R = 1\,, \quad \gamma = 1.4\,, \quad g = 1\,, \quad u = v = w = 0\,, \tag{58}$$

inside the domain $[0, 1]$. The numerical schemes must preserve this hydrostatic equilibrium with machine precision. We compute the solution at $t = 0.8$ using the TENO-3, TENO-5 and TENO-7 reconstruction using 80, 160 and 320 cells.

Table 1 shows the deviation in the computed pressure and vertical velocity from the equilibrium state, for the case of 160 cells, measured with the L_1 norm, which is defined as

$$L_1(p) = \sum_{k=1,\dots,N_z} \left|p_k - p^e_k\right|\Delta z\,, \quad L_1(w) = \sum_{k=1,\dots,N_z} \left|w_k - w^e_k\right|\Delta z. \tag{59}$$

As observed in Table 1, the computed solutions preserve the initial equilibrium with machine accuracy (double precision). Numerical errors are of the order of 10^{-14}.

Table 1
Numerical errors for p and w measured using the L_1 norm.

Scheme	$L_1(p)$	$L_1(w)$
TENO-3	1.02e-14	8.75e-14
TENO-5	1.02e-14	8.72e-14
TENO-7	1.02e-14	7.22e-14

Table 2
Magnitude of the correction of the integral of the source term.

N_z	$L_1(\varphi)$		
	TENO-3	TENO-5	TENO-7
80	8.54e-04	6.67e-07	5.58e-10
320	5.80e-05	2.83e-09	3.96e-13

Table 3
Convergence rates for ρ at $t = 0.8$ setting $\eta = 0.01$, computed with the L_1 error norms.

Meshes (N_j/N_{j+1})	TENO-3		TENO-5		TENO-7	
	$L_1(\rho)$	$\mathcal{O}_{L_1}$	$L_1(\rho)$	$\mathcal{O}_{L_1}$	$L_1(\rho)$	$\mathcal{O}_{L_1}$
40/80	1.34e-04	-	1.16e-04	-	1.29e-04	-
80/160	8.72e-05	0.62	5.01e-05	1.21	3.67e-05	1.82
160/320	3.52e-05	1.31	7.97e-06	2.65	2.13e-06	4.11
320/640	9.18e-06	1.94	3.85e-07	4.37	3.01e-08	6.14
640/1280	1.57e-06	2.54	1.29e-08	4.90	2.79e-10	6.75
1280/2560	2.66e-07	2.57	4.12e-10	4.97	7.70e-12	5.18

To evidence the role of the correction of the integral of the source term in Equation (57), φ_k, we show in Table 2 the magnitude of this term for the TENO reconstruction, measured with the following L_1 norm

$$L_1(\varphi) = \sum_{k=1+nb,\dots,N_z-nb} |\varphi_k| \Delta z \,, \tag{60}$$

where nb represents the number of boundary cells which are not considered, since the polynomial order decreases in those cells.

The magnitude of the correction term decreases with the number of cells and the order of the numerical scheme, as the accuracy of the reconstruction of ρ^e and p^e increases. When using the 7-th order TENO scheme with 320 cells, $L_1(\varphi)$ is close to machine precision, evidencing that the correction term would not be necessary when using very high order schemes in fine grids [6]. However, the combination of a fine grid and a very high order of accuracy may be unpractical in terms of computational cost, motivating the need of well-balancing [4].

4.2. Case 2. Perturbation over the one-dimensional isothermal steady state

We consider the hydrostatic isothermal equilibrium in Equation (8), setting as initial condition [18,31,62]

$$p(z,0) = p^e(\hat{z}) + \eta \exp\left(-100(\hat{z}-0.5)^2\right), \quad \rho(z,0) = \rho^e(\hat{z}), \quad \mathbf{v}(z,0) = 0 \tag{61}$$

with η the amplitude of the perturbation, $\hat{z} = z - 2$ and

$$\rho_0 = 1\,, \quad p_0 = 1\,, \quad R = 1\,, \quad \gamma = 1.4\,, \quad g = 1\,, \quad u = v = w = 0\,, \tag{62}$$

inside the spatial domain $z = [0, 5]$. We consider two different cases setting $\eta = 0.01$ and $\eta = 10^{-8}$ and compute the solution at $t = 0.8$ setting the CFL number to 0.05.

Table 3 shows a convergence rate test for the schemes using the TENO-3, TENO-5 and TENO-7 reconstruction, setting $\eta = 0.01$. The order of convergence of the schemes is estimated using the double-mesh principle. The following set of meshes are considered: $N_l = \{20, 40, 80, 160, 320, 640\}$. For two arbitrary meshes $\mathcal{M}1$ and $\mathcal{M}2$, the L_1 norm of the difference of the computed ρ in such meshes is calculated as:

$$L_1(\rho) = \sum_{k=1}^{N_{\mathcal{M}1}} \left| 0.5\left(\{\rho^n_{2k}\}_{\mathcal{M}2} + \{\rho^n_{2k-1}\}_{\mathcal{M}2}\right) - \{\rho^n_k\}_{\mathcal{M}1} \right| \Delta z \,, \tag{63}$$

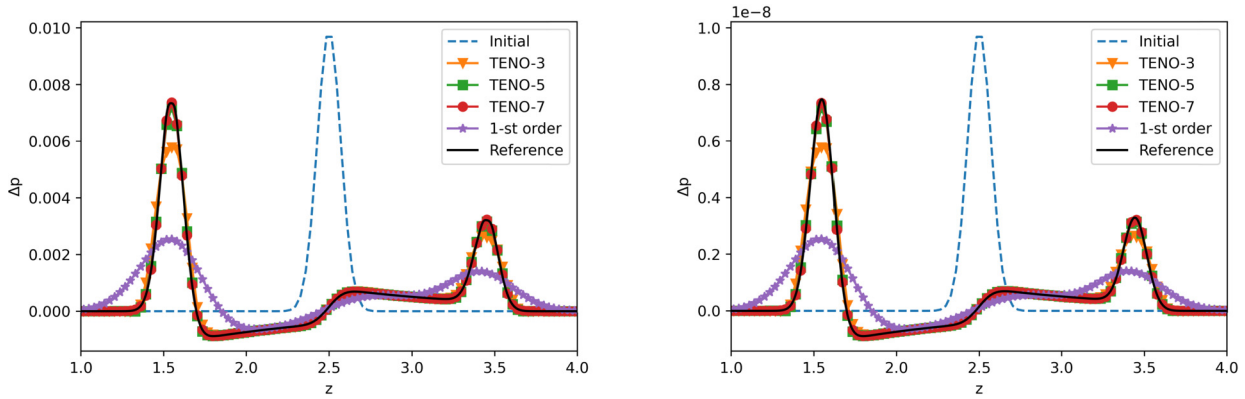

Fig. 2. Case 2. Numerical solution for the pressure perturbation ($\Delta p = p - p^e$) at $t = 0.8$ setting $\eta = 0.01$ (left) and $\eta = 10^{-8}$ (right).

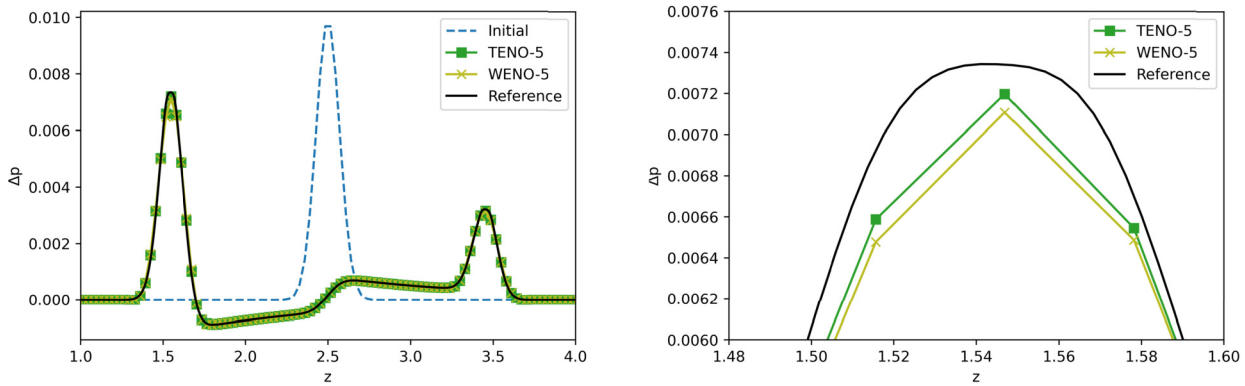

Fig. 3. Case 2. Numerical solution for the pressure perturbation ($\Delta p = p - p^e$) at $t = 0.8$ setting $\eta = 0.01$. Full domain (left) and detail of the left-moving gravity wave (right).

Table 4
Location and amplitude of the left and right moving waves (denoted by 1 and 2, respectively). The values marked with $^{(*)}$ have been extracted from the corresponding papers using a digitizer tool, therefore only two significant digits after the comma are displayed.

Scheme	N	η	t	x_1	x_2	Δp_1	Δp_2
TENO-7	1280	10^{-8}	0.8	1.5488	3.4434	7.47e-9	3.29e-9
Li and Gao, 2021 [31]	28350	10^{-8}	0.8	$1.55^{(*)}$	$3.44^{(*)}$	$7.5e\text{-}9^{(*)}$	$3.3e\text{-}9^{(*)}$
TENO-7	1280	10^{-2}	0.25	2.1972	2.7949	5.44e-3	4.58e-3
Ghosh and Constantinescu, 2016 [18]	2000	10^{-2}	0.25	$2.20^{(*)}$	$2.79^{(*)}$	$5.4e\text{-}3^{(*)}$	$4.6e\text{-}3^{(*)}$

with $\{\rho_l^n\}_{\mathcal{M}_l}$ stands for the cell-averaged density at time t^n computed in the grid $\mathcal{M}_l$. Table 3 shows that the TENO-5 and TENO-7 schemes achieve the theoretical convergence rates, whereas the TENO-3 scheme is slightly suboptimal for the grids herein considered.

The numerical solution for the pressure perturbation setting $\eta = 0.01$ and $\eta = 10^{-8}$ is depicted in Fig. 2. The solution is computed using the 1-st order scheme, as well as the TENO-3, TENO-5 and TENO-7 reconstruction with $N = 160$ cells. The reference solution is computed using the TENO-7 scheme with $N = 1280$ cells. The proposed scheme is able to capture the propagation of the gravity waves produced by the initial perturbation with high accuracy. Some numerical diffusion smearing the solution is observed for the 3-rd order scheme, specially when choosing $\eta = 0.01$. Fig. 3 shows the numerical solution for the pressure perturbation with amplitude $\eta = 0.01$, provided by the 5-th order WENO-JS and TENO reconstructions. Both methods render similar results, being the TENO-5 scheme slightly less diffusive. The results in Figs. 2 and 3 are in good agreement with those reported in previous literature [18,31]. In Table 4, the location and amplitude of the left and right moving waves, provided by the TENO-7 scheme in a very fine grid, are compared with previous results from the literature. Our results are in very good agreement with those by Ghosh and Constantinescu [18] and by Li and Gao [31].

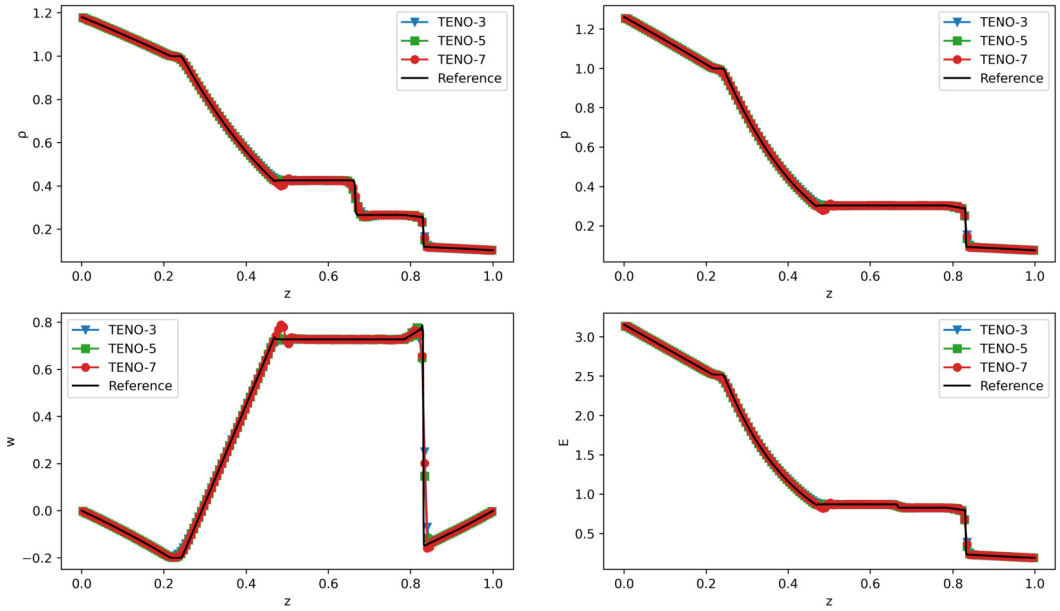

Fig. 4. Case 3. Computed density (top-left), pressure (top-right), vertical velocity (bottom left) and total energy (bottom right) at $t = 0.2$ using 160 cells.

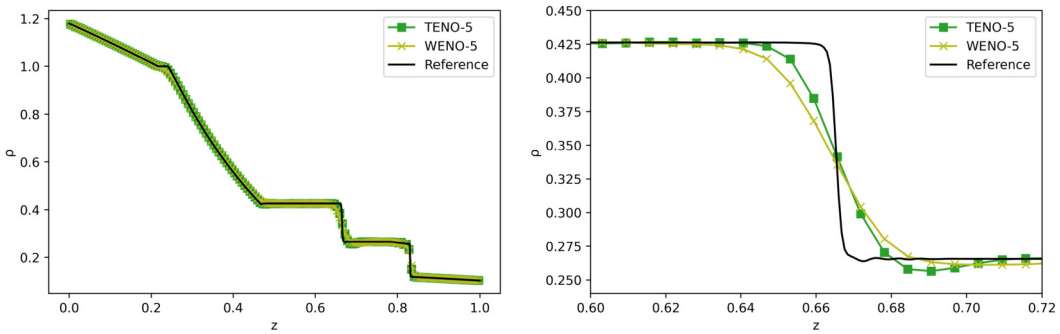

Fig. 5. Case 3. Computed density at $t = 0.2$ using 160 cells with a WENO-5 and TENO-5 scheme.

4.3. Case 3. Sod's shock tube with gravitational forcing

Here we consider a modification of the traditional Sod problem by means of a gravitational force with $g = 1$, setting as background equilibrium state the isothermal equilibrium in Equation (8) with

$$\rho_0 = 1\,, \quad p_0 = 1\,, \quad R = 1\,, \quad \gamma = 1.4\,. \tag{64}$$

Following [18,31,62], the initial condition is given by the following piecewise constant data

$$(\rho, u, p) = \begin{cases} (1, 0, 1) & \text{if} \quad z \leq 0.5 \\ (0.125, 0, 0.1) & \text{if} \quad z > 0.5 \end{cases} \tag{65}$$

inside the domain $[0, 1]$. The solution is computed at $t = 0.2$ using the schemes based on the TENO-3, TENO-5 and TENO-7 reconstruction inside a mesh with 160 cells and a CFL number of 0.4. We also compute a reference solution in a fine mesh (1280 cells) using the TENO-7 scheme. The solutions are presented in Fig. 4, showing that all the schemes accurately capture the waves arising from the discontinuous initial condition. The numerical results evidence that the proposed schemes are able to handle discontinuous solutions such as shocks and contact waves, providing essentially non-oscillatory solutions. Only the TENO-7 reconstruction shows small oscillations at the tail of the rarefaction wave ($x \approx 0.45$), which could be reduced by adjusting the value of C_T.

Fig. 5 shows a comparison of the numerical solution provided by the WENO-5 and TENO-5 schemes. The accuracy of both methods near discontinuities is similar, being the TENO-5 scheme slightly less diffusive.

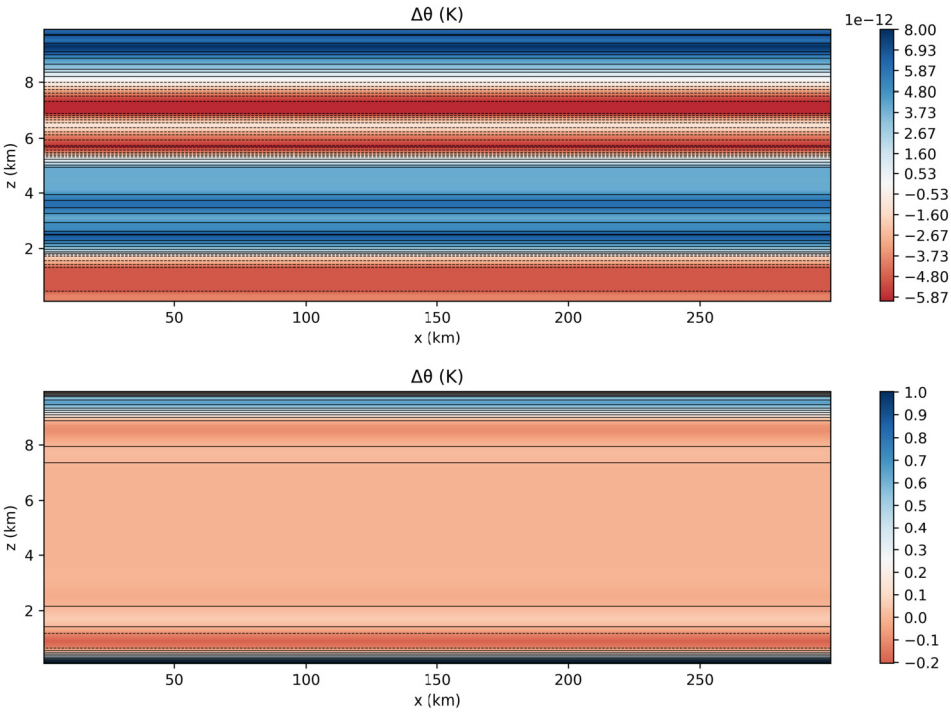

Fig. 6. Case 4. Potential temperature perturbation at $t = 200$ s, setting as initial condition the hydrostatic equilibrium state, computed by the 5-th order TENO scheme using the HLLS solver (top) and the original HLL solver (bottom). (For interpretation of the colors in the figure(s), the reader is referred to the web version of this article.)

4.4. Case 4. Inertia-gravity waves

This test case was introduced by Skamarock and Klemp [52] and involves the propagation of inertia-gravity waves in a horizontal channel defined in the domain $\Omega = [0, 300] \times [0, 10]$ km^2, with solid walls along the bottom and top boundaries and cyclic boundary conditions on the left and right boundaries. The flow is triggered by an initial perturbation over an stratified atmosphere in hydrostatic equilibrium with a constant Brunt-Väisälä frequency of $\mathcal{N} = 0.01$ s^{-1}. The equilibrium state is given in Equations (10)-(12), where

$$p_0 = 10^5 \text{ Pa}, \quad T_0 = 300 \text{ K}, \quad R = 287.058 \text{ kJ/kg K}, \quad \gamma = 1.4, \quad g = 9.8 \text{ m/s}^2 \tag{66}$$

and a constant horizontal wind of $u = 20$ m/s. To generate the inertia-gravity waves, we introduce the following perturbation for the potential temperature

$$\Delta\theta = \theta_c \frac{\sin\left(\frac{\pi_c z}{h_c}\right)}{\left(1 + \left(\frac{x - x_c}{a_c}\right)^2\right)} \tag{67}$$

with $\theta_c = 0.01$ K the amplitude of the perturbation, $h_c = 10000$ m the height of the domain, $a_c = 5000$ m the perturbation half-width, $x_c = 100000$ m the center of the perturbation and π_c the trigonometric constant [52]. As in [18], we consider a resolution of $\Delta x = 250$ m and $\Delta z = 200$ m. The CFL number is set to 0.49.

To assess the performance of the proposed scheme to preserve this particular equilibrium state involving velocity in the horizontal direction, we have computed the solution at $t = 200$ s setting as initial condition the equilibrium state. Fig. 6 shows the perturbation of potential temperature at $t = 200$ s computed by the 5-th order TENO scheme using the HLLS solver and the original HLL solver, which is not well-balanced. We observe that the proposed solver ensures the well-balanced property when dealing with non-zero horizontal velocities.

Now, the evolution of the perturbation is computed at $t = 3000$ s using the WENO, TENO and linear schemes of 3-rd, 5-th and 7-th order. Fig. 7 shows the solution for the potential temperature perturbation provided by the 7-th order TENO scheme. The cross sectional potential temperature perturbation at $z = 5000$ m is displayed in Fig. 8, showing that all the schemes provide similar results with independence of the order of accuracy. The solutions are compared with a reference solution of the NUMA code used in [18], showing a good agreement. Small differences are observed at the local extrema, due to the numerical viscosity of the HLLS solver. On the other hand, Fig. 9 shows the cross sectional potential temperature

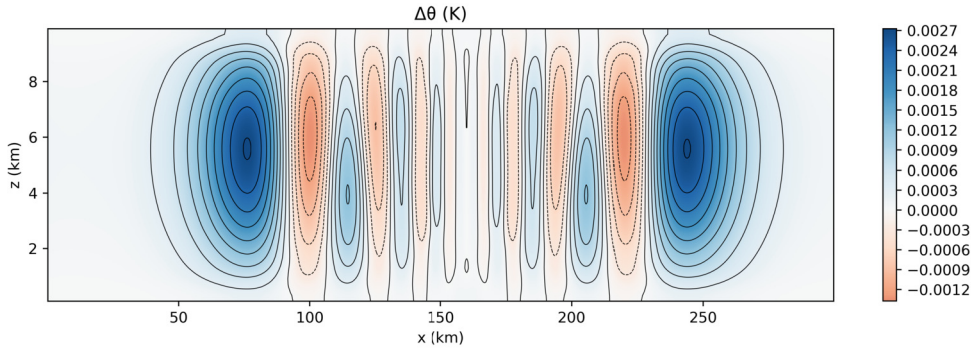

Fig. 7. Case 4. Potential temperature perturbation at $t = 3000$ s computed by the 3-rd (top) and 7-th order TENO scheme.

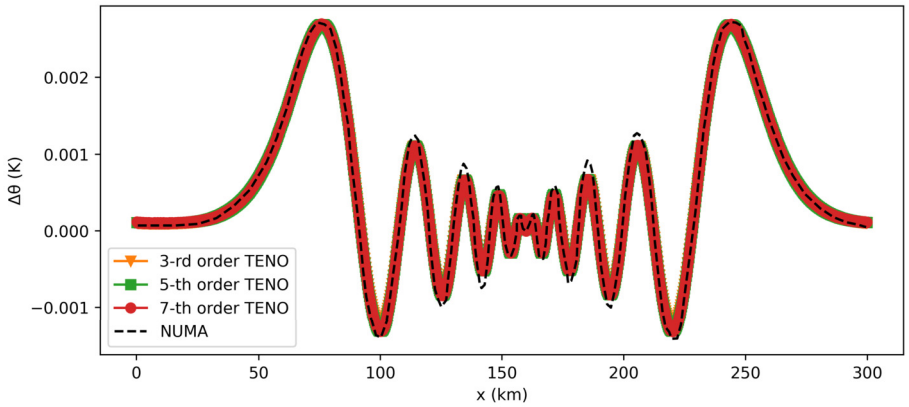

Fig. 8. Case 4. Potential temperature perturbation at $t = 3000$ s computed by the 3-rd, 5-th and 7-th order TENO scheme, and compared with a reference solution from [18].

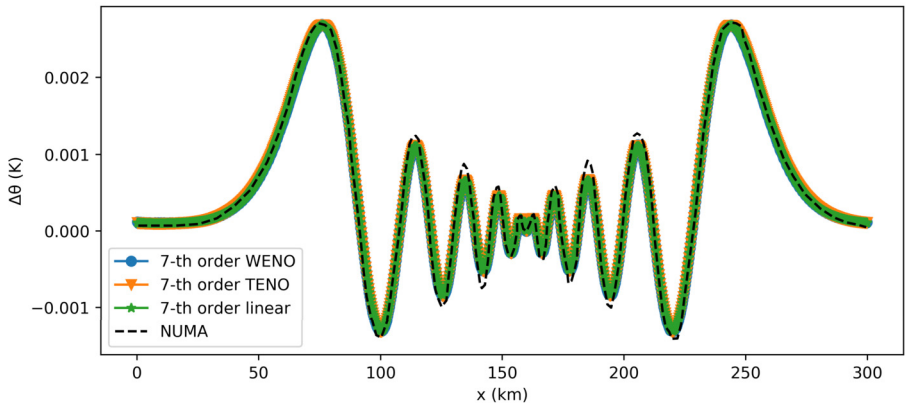

Fig. 9. Case 4. Potential temperature perturbation at $t = 3000$ s computed by the 7-th order WENO, TENO and linear schemes, and compared with a reference solution from [18].

perturbation computed by the 7-th order WENO, TENO and linear schemes. In this case, the 3 different spatial reconstruction methods provide similar results since the solution is very smooth.

4.5. Case 5. 2D rising thermal bubble

Here we consider the 2D rising thermal bubble proposed by Robert [47] with the configuration by Giraldo and Restelli [19]. This test case and its derivatives are a standard benchmark for the NWP community [19,23,57,33,38,46,30,60]. It involves the ascent of a warm bubble in the form of a perturbation of potential temperature, which produces a vertical acceleration. In the beginning of the simulation, the bubble smoothly rises vertically. At later stages, the velocity gradients produced by the differences of potential temperature deform the bubble to a mushroom-like cloud with two counter-

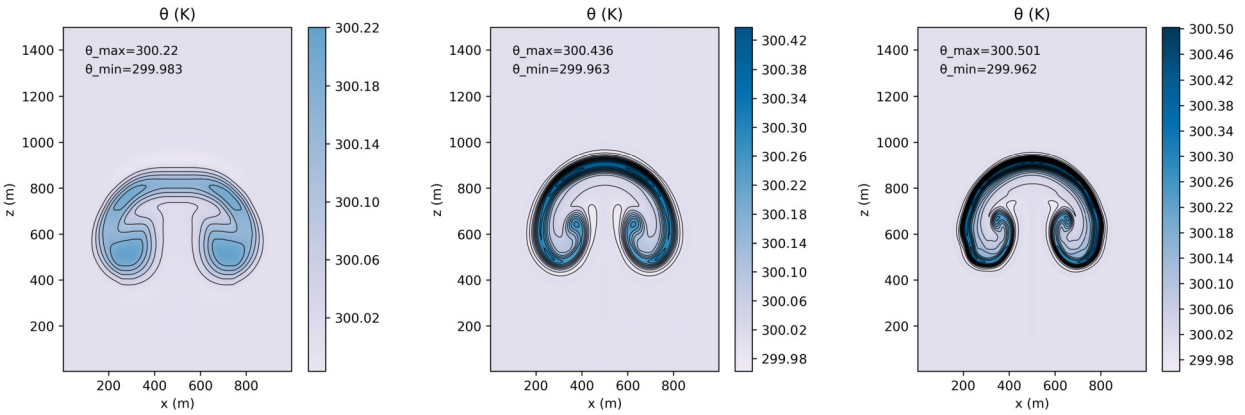

Fig. 10. Case 5. Computed potential temperature at $t = 700$ s using $\Delta x = 5$ m cells with a TENO-3 (left), TENO-5 (middle) and TENO-7 scheme (right).

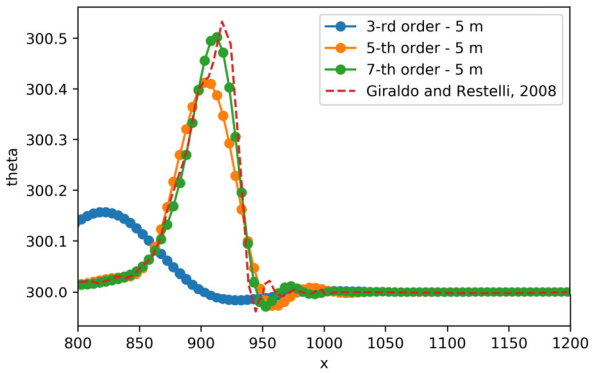

Fig. 11. Case 5. Potential temperature vertical profile at $t = 700$ s using $\Delta x = 5$ m cells computed with the TENO reconstruction.

rotating trailing vortices [18]. The background temperature is 300 K whereas the maximum perturbation inside the bubble is 0.5 K. The evolution of such a subtle perturbation for a long simulation time makes the solution be very sensitive to the numerical scheme, being strongly affected by numerical diffusion. Therefore, we will use this test case to assess the performance of the proposed scheme based on the TENO reconstruction.

For this case, the background equilibrium state is the adiabatic equilibrium in Equation (9) with

$$p_0 = 10^5 \text{ Pa}, \quad \theta_0 = 300 \text{ K}, \quad R = 287.058 \text{ kJ/kg K}, \quad \gamma = 1.4, \quad g = 9.8 \text{ m/s}^2 \tag{68}$$

The problem is defined inside the domain $[0, 1000] \times [0, 1500]$ m^2. To drive the motion, we add a perturbation in the potential temperature [19]

$$\Delta\theta = \begin{cases} 0 & \text{if} \quad r > r_c \\ \frac{\theta_c}{2}\left(1 + \cos\left(\frac{\pi r}{r_c}\right)\right) & \text{if} \quad r \leq r_c \end{cases} \tag{69}$$

with $\theta_c = 0.5$ K, $r_c = 250$ m and

$$r = \sqrt{(x - x_c)^2 + (z - z_c)^2} \tag{70}$$

where $(x_c, y_c) = (500, 260)$ m.

The perturbation in (69) is introduced as $\theta = \theta_0 + \Delta\theta$. The initial condition for the pressure and density can be computed as follows

$$p = p_0 \left(1 - \frac{(\gamma - 1) g z}{\gamma R \theta_0}\right)^{\frac{\gamma}{\gamma - 1}}, \quad \rho = \frac{p_0}{R\theta} \left(1 - \frac{(\gamma - 1) g z}{\gamma R \theta_0}\right)^{\frac{1}{\gamma - 1}}, \tag{71}$$

with p_0, R, g and γ defined in Equation (68).

The solution is computed using the proposed scheme inside a mesh with $\Delta x = \Delta z = 5$ m and a CFL number of 0.49. Fig. 10 shows the computed potential temperature at $t = 700$ s with the 3-rd, 5-th and 7-th order TENO reconstructions. Additionally, a vertical profile of the computed potential temperature is presented in Fig. 11 and compared with a reference

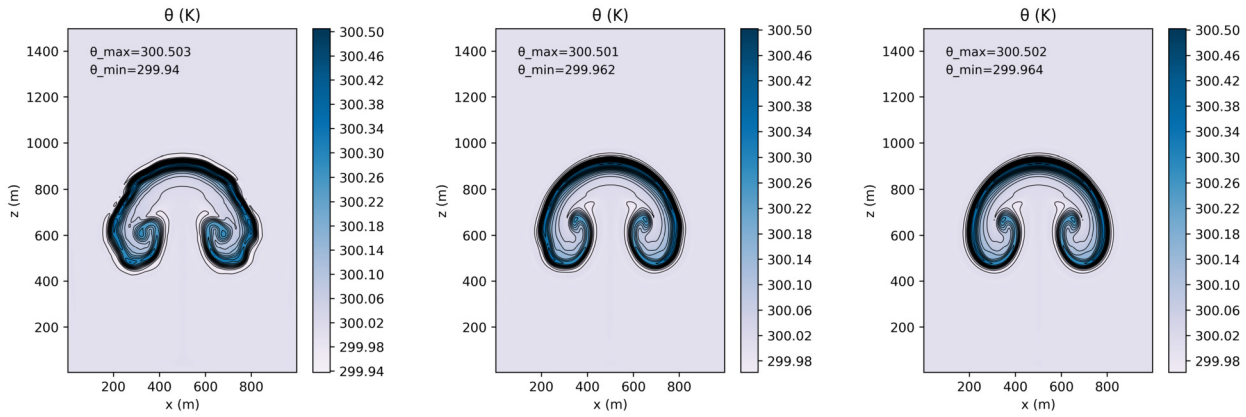

Fig. 12. Case 5. Computed potential temperature at $t = 700$ s using $\Delta x = 5$ m cells with a 7-th order WENO-JS (left), TENO (middle) and linear scheme (right).

solution from [19]. From these figures, we observe that the solution is very sensitive to the order of accuracy. The 3-rd order scheme is too diffusive and hence not adequate for this problem, whereas the 5-th and 7-th order schemes adequately reproduce the mushroom-shaped ascending cloud. Fig. 11 shows that the solution provided by the 7-th order TENO scheme is in very good agreement with the reference solution in [19]. It is worth noting that small spurious oscillations appear on the upper front of the bubble, although the reconstruction method is essentially non-oscillatory. This evidences the complexity of this test case and motivates its use for a deep assessment of the methods. This issue will be further discussed later.

To investigate the sensitivity of the solution to the reconstruction scheme, the solution is computed with different methods, i.e. WENO-JS, TENO and linear reconstructions. Fig. 12 shows the computed potential temperature at $t = 700$ s provided by the WENO-JS, TENO and linear reconstruction. The results evidence that the solution is very sensitive to the reconstruction scheme. The traditional WENO-JS reconstruction produces a distortion of the bubble, whereas the TENO and linear reconstruction provide smoother solutions. We believe that such a distortion is produced by the weighted stencil selection featured by the WENO-JS method (original Jiang-Shu weights).

The evolution in time of the solution provided by the TENO-7 reconstruction is presented in Fig. 13, showing the computed potential temperature at different times from $t = 0$ s to $t = 900$ s. As reported by other authors [18], the spectral properties of the reconstruction method play a key role in the features of the trailing edges of the bubble. To investigate this aspect, we have computed the solution at $t = 900$ with the TENO scheme using different values of C_T in Equation (32). This parameter represents the threshold for the ENO-based stencil selection and determines the robustness and spectral resolution of the scheme [14]. Fig. 14 shows the computed potential temperature at $t = 900$ s using $\Delta x = 5$ m cells with a TENO-7 scheme using $C_T = 10^{-5}$, $C_T = 10^{-6}$, $C_T = 10^{-7}$, $C_T = 10^{-8}$. For $C_T = 10^{-5}$, the shape of the bubble is perturbed, both on the top and on the trail edges, and multiple vortical structures are shed around the trailing edges. In relation to this, Savre et al. [49] reported that in presence of anisotropic numerical diffusion, the shape of the rising thermal may be deteriorated. Decreasing C_T, the spectral resolution is increased and the solution converges to that of the linear reconstruction (optimal polynomial reconstruction). For $C_T = 10^{-7}$ and $C_T = 10^{-8}$, the solution is virtually equal. A compromise between spectral resolution and robustness must be sought when choosing the value of C_T.

As pointed out by Andres-Carcasona et al. [2], the perturbation should not go over the initial maximum (i.e. 300.5 K) or below the initial minimum (i.e. 300 K) since there is no physical source or sink of energy. However, overshooting of the potential temperature has been reported in the literature by multiple authors. Savre et al. [49] pointed out that even when using slope limiters and/or artificial viscosity, potential temperature overshoots can appear. Fig. 15 shows the evolution in time of the maximum potential temperature in the domain for the TENO reconstruction of order 3, 5 and 7 using $C_T = 10^{-6}$ as well as for the TENO-7 reconstruction using different values of C_T. As mentioned before, the TENO-3 reconstruction shows an excessive numerical diffusion, damping the solution from the beginning. The TENO-5 reconstruction is less diffusive but it still damps the solution after $t = 450$ s. On the other hand, the TENO-7 reconstruction does not show any attenuation of the solution but a slight overshooting above 300.5 K. It is worth noting that a higher value of C_T (i.e. a more restrictive limitation for the stencil selection in the spatial reconstruction) does not produce a significant reduction of the overshooting in this case.

4.6. Case 6. 2D colliding thermals

The colliding thermals test case, recently proposed by Norman [42], involves the collision of two thermal bubbles moving in opposite directions, which produce strong gradients of potential temperature. It was designed to evidence the performance of the schemes when handling strong winds, strong turbulence and sharp gradients.

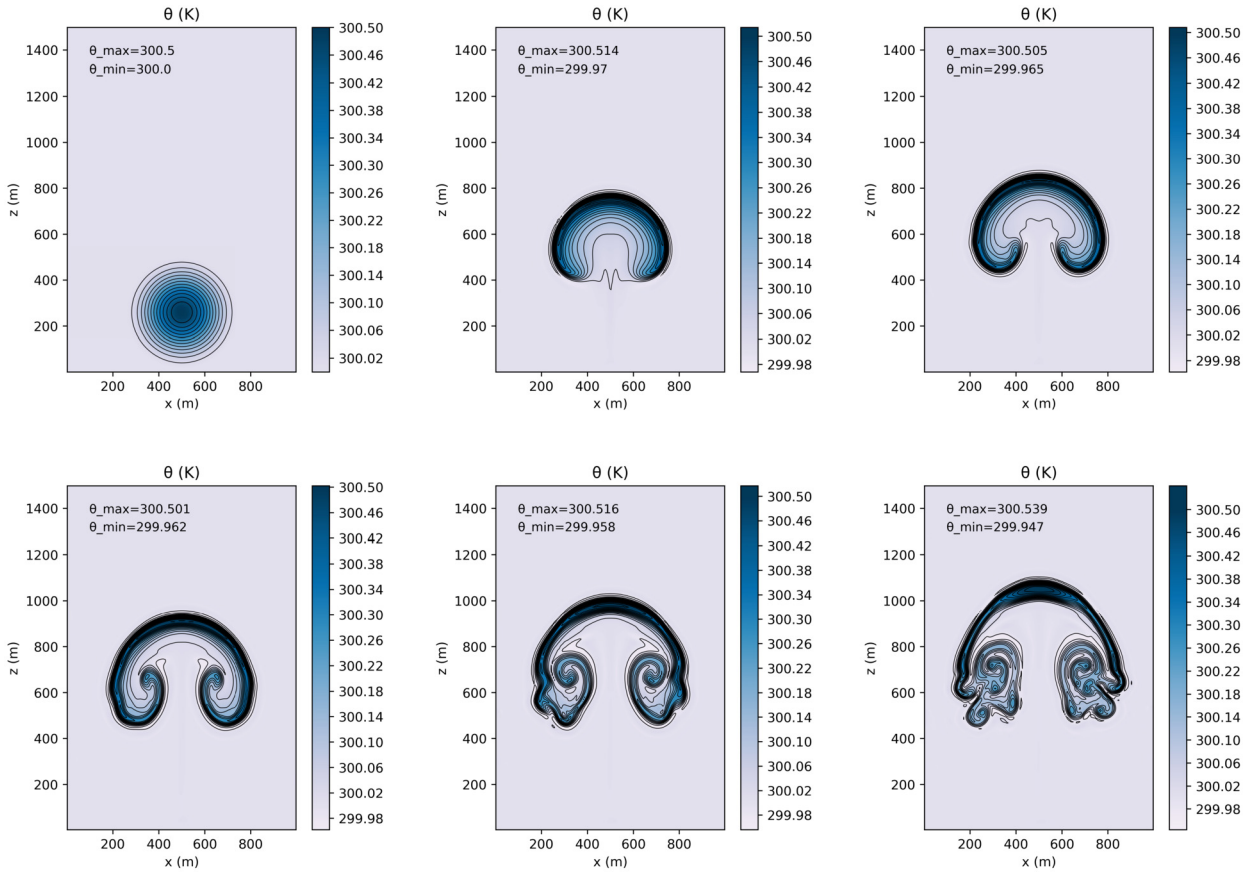

Fig. 13. Case 5. Computed potential temperature at $t = \{0, 500, 600, 700, 800, 900\}$ s using $\Delta x = 5$ m cells with a TENO-7 reconstruction.

For this case, the background equilibrium state is the adiabatic equilibrium in Equation (9) with

$$p_0 = 10^5 \text{ Pa}, \quad \theta_0 = 300 \text{ K}, \quad R = 287.058 \text{ kJ/kg K}, \quad \gamma = 1.4, \quad g = 9.8 \text{ m/s}^2 \tag{72}$$

and with no winds, $u = v = w = 0$.

The problem is defined inside the domain $[0, 20000] \times [0, 10000]$ m^2. To drive the motion, we add a perturbation in the potential temperature

$$\Delta\theta = 20(\max(1 - d_1, 0) + \min(d_2 - 1, 0)); \tag{73}$$

with

$$d_1 = \frac{\sqrt{(x - x_1)^2 + (z - z_1)^2}}{r}, \quad d_2 = \frac{\sqrt{(x - x_2)^2 + (z - z_2)^2}}{r}, \tag{74}$$

where $r = 2000$ m is the radius of the bubbles, $(x_1, z_1) = (10000, 2000)$ m is the center of the warm bubble and $(x_2, z_2) = (10000, 8000)$ m is the center of the cold bubble. The solution is computed with the proposed scheme using a resolution of $\Delta x = \Delta z = 50$ m. Fig. 16 shows the potential temperature computed by the 7-th order TENO scheme at $t = 200$ s, $t = 300$ s, $t = 400$ s and $t = 700$ s. Note that $C_T = 10^{-6}$ is used again. These results are qualitatively similar to those in [42]. A profile of the computed potential temperature by the 7-th order WENO-JS, TENO and linear scheme at $t = 300$ s along the z direction at $x = 10000$ m is also displayed in Fig. 17. Note that the TENO scheme and its linear counterpart provide similar results, while the WENO-JS scheme is more diffusive. In [42], Norman observed that the linear scheme produces spurious oscillations across the discontinuity at $z = 5000$ m, whereas our results in Fig. 17 do not show such features. The reason may be that the HLLS solver introduces higher numerical viscosity than the flux formulation in [42], thus smearing out the discontinuity even when no limiter is used (i.e. linear reconstruction). To evidence the eddy-resolving capabilities of the proposed scheme, we show in Fig. 18 the computed potential temperature at $t = 400$ s using the 7-th order TENO scheme in a finer mesh ($\Delta x = \Delta z = 10$ m). The vortical structures due to the Kelvin-Helmholtz shear instability are reproduced.

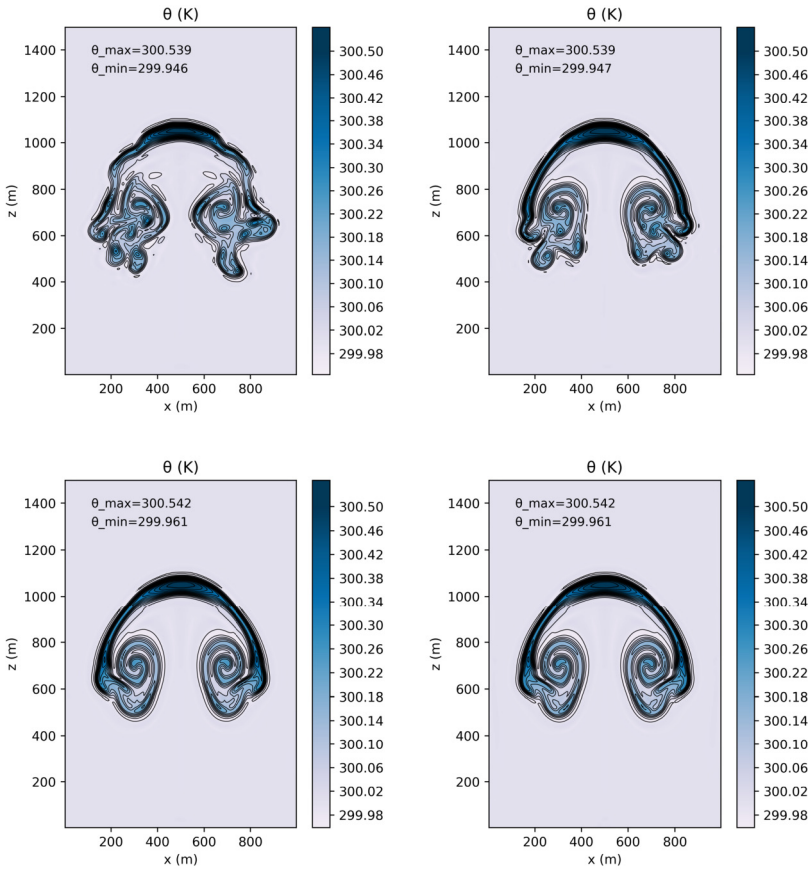

Fig. 14. Case 5. Computed potential temperature at $t = 900$ s using $\Delta x = 5$ m cells with a TENO-7 scheme using $C_T = 10^{-5}$ (top left), $C_T = 10^{-6}$ (top right), $C_T = 10^{-7}$ (bottom left), $C_T = 10^{-8}$ (bottom right).

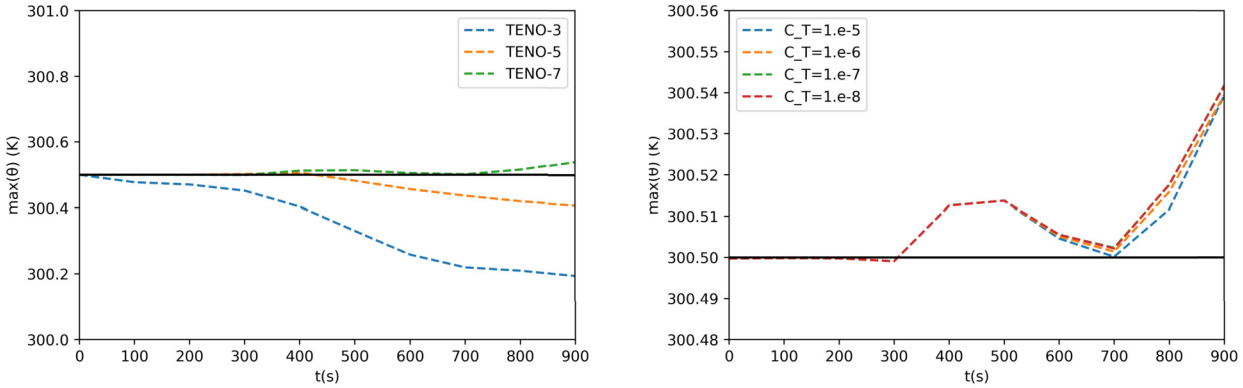

Fig. 15. Case 5. Maximum potential temperature for the TENO schemes using $C_T = 10^{-6}$ (left) and for the TENO-7 scheme using different values of C_T (right).

4.7. Case 7. 2D strong colliding thermals

This test case is designed to evidence the advantages of non-linear limiting (i.e. WENO and TENO methods) versus a linear reconstruction when performing high-order spatial reconstructions. It is similar to Case 6, with the equilibrium given by (9) and (72), but stronger gradients of potential temperature are sought by defining the following potential temperature perturbation

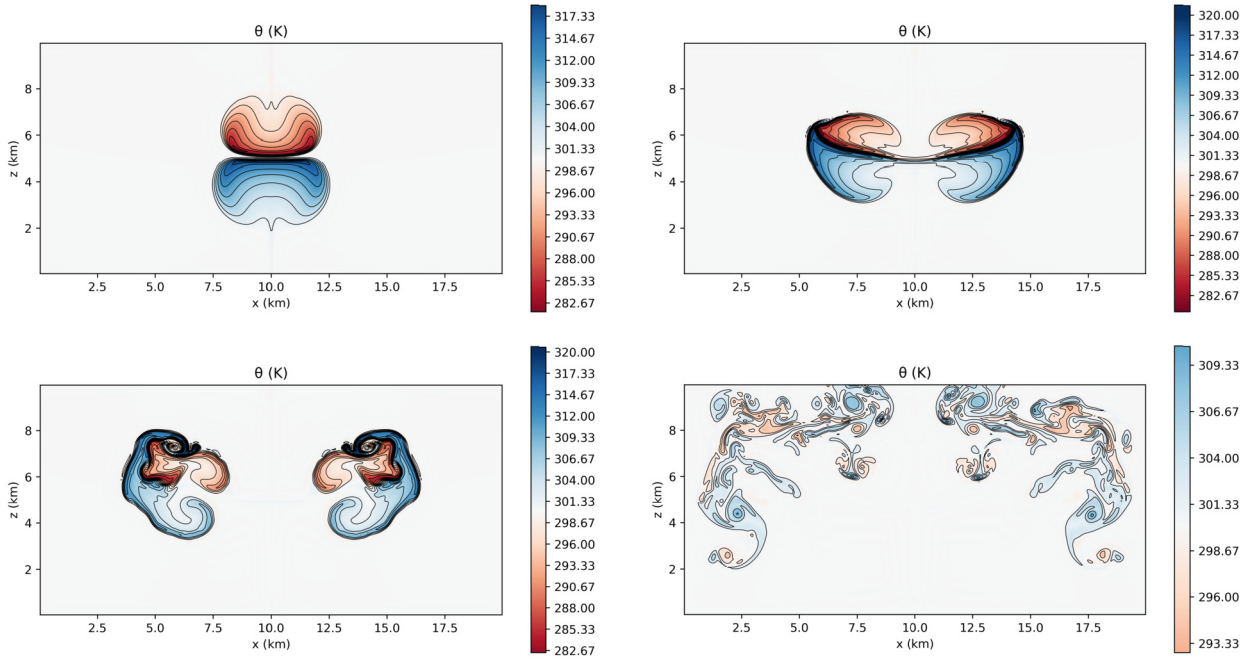

Fig. 16. Case 6. Computed potential temperature by the 7-th order TENO scheme ($C_T = 10^{-6}$) at $t = 200$ s, $t = 300$ s, $t = 400$ s and $t = 700$ s.

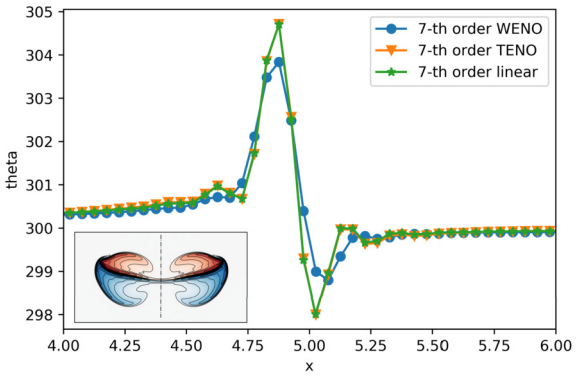

Fig. 17. Case 6. Computed potential temperature along the z direction at $t = 300$ s and $x = 10000$ m.

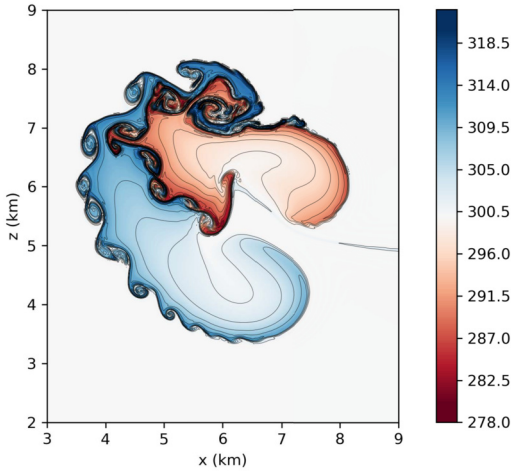

Fig. 18. Case 6. Computed potential temperature at $t = 400$ s using the 7-th order TENO scheme ($C_T = 10^{-6}$) in a fine mesh.

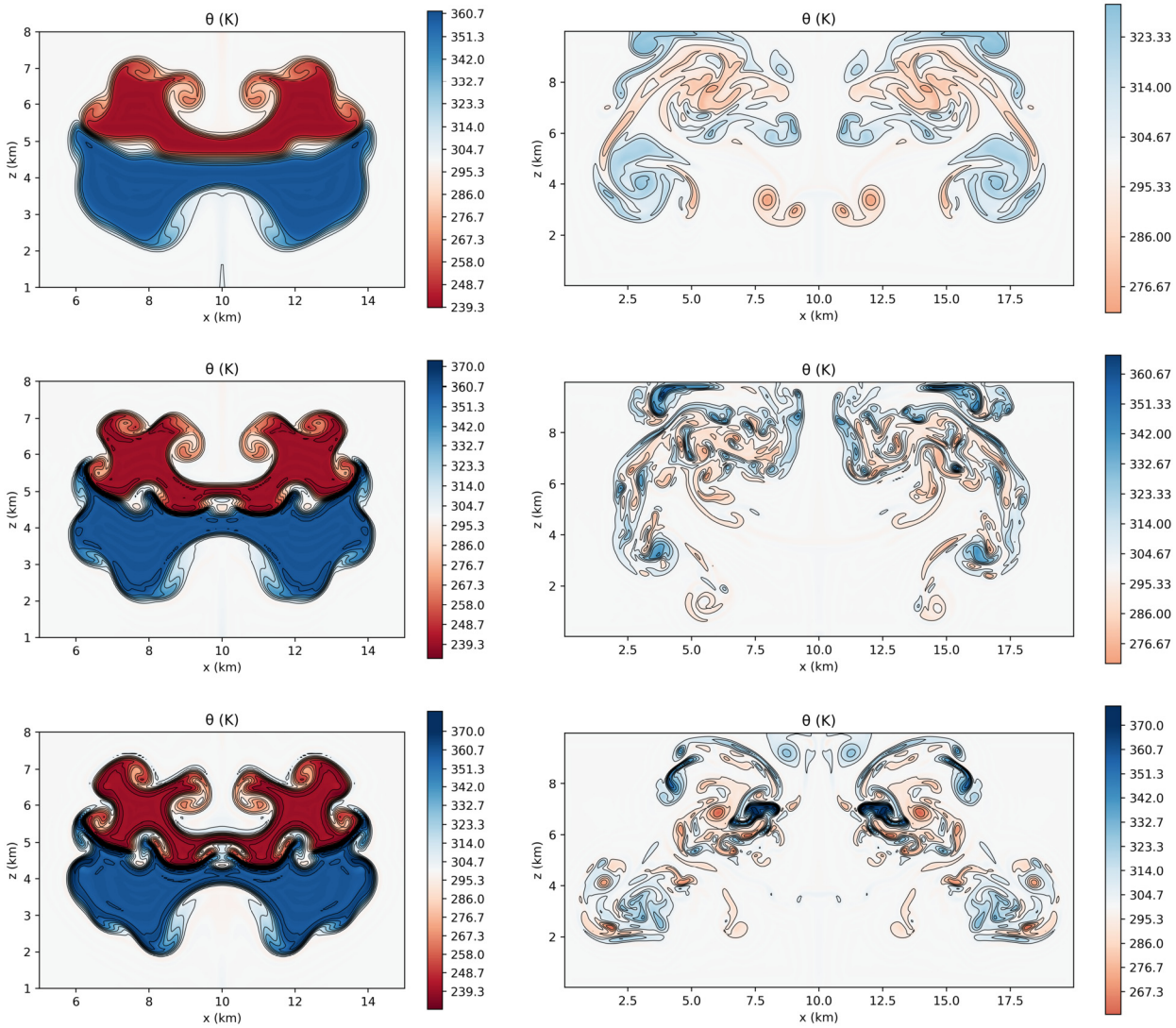

Fig. 19. Case 7. Computed potential temperature at $t = 100$ s (left) and $t = 280$ s (right) using the WENO (top), TENO ($C_T = 10^{-6}$) (middle) and linear scheme (bottom).

$$\Delta\theta = \begin{cases} 60 & \text{if} \quad 1 - d_1 > 0 \\ -60 & \text{if} \quad d_2 - 1 < 0 \\ 0 & \text{otherwise} \end{cases} \tag{75}$$

with d_1 and d_2 computed as in (74). Note that the bubbles are defined as discontinuous circular regions with a potential temperature perturbation of 60 K.

The solution is computed with the proposed scheme using a resolution of $\Delta x = \Delta z = 50$ m. Fig. 19 shows the potential temperature field computed using the 5-th order WENO-JS, TENO and linear reconstructions at $t = 100$ s and $t = 280$ s. Due to the sharp edges of the bubbles, Kelvin-Helmholtz instabilities are formed along them. The WENO-JS method shows a higher numerical diffusion, smearing out the gradients along the boundaries and only capturing the largest eddies. On the contrary, TENO and linear reconstructions are able to resolve smaller eddies. At $t = 280$ s, the solution evolves into a fully turbulent field. The numerical results evidence that the TENO and linear reconstructions can capture smaller vortical structures than the WENO-JS reconstruction, resolving a larger extent of the energy spectrum.

To motivate the actual importance of the reconstruction scheme in the solution, a cross-sectional representation of the potential temperature in the z direction at $x = 8925$ m and $t = 100$ s is provided in Fig. 20. We only show the region where the fronts collide. Different values of C_T have been considered for the TENO reconstruction to assess the robustness of the method. The WENO-JS and TENO reconstruction using higher values of C_T (i.e. $C_T = 10^{-7}$ and higher) are able to capture the sharp interface without spurious oscillations, however, the linear reconstruction and the TENO reconstruction with lower values of C_T (i.e. $C_T = 10^{-8}$ and lower) exhibit strong spurious oscillations (Gibbs phenomenon). To better

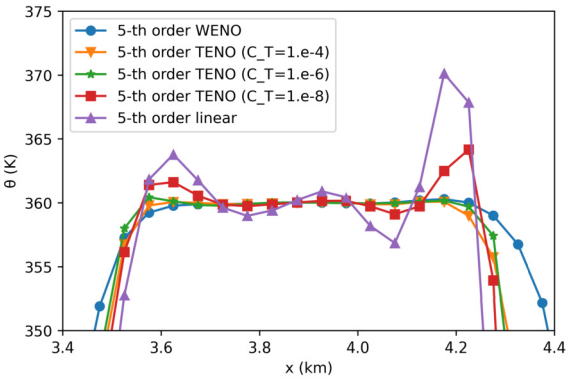

Fig. 20. Case 7. Computed potential temperature along the z direction at $x = 8925$ m.

Table 5
Maximum and minimum potential temperature in the solution at $t = 100$ s.

Scheme	max (θ) (K)	min (θ) (K)
WENO-JS	360.87	239.60
TENO ($C_T = 10^{-3}$)	361.97	237.82
TENO ($C_T = 10^{-4}$)	365.18	237.38
TENO ($C_T = 10^{-5}$)	370.68	233.26
TENO ($C_T = 10^{-6}$)	372.72	233.10
TENO ($C_T = 10^{-7}$)	375.99	232.75
TENO ($C_T = 10^{-8}$)	375.14	231.80
Linear reconstruction	379.83	230.50

examine the overshooting of the potential temperature in the solution, a more suitable indicator is the measure of the absolute maximum and minimum potential temperature in the domain [2]. In Table 5 we display the absolute extrema of the computed potential temperature at $t = 100$ s. As expected, only the WENO and TENO reconstruction with a high value of C_T (i.e. $C_T = 10^{-3}$) virtually damp the spurious oscillations in the whole domain. On the other hand, the linear reconstruction exhibits large overshooting. It is clearly evidenced how the choice of C_T for the TENO reconstruction allows controlling the robustness of the method. Fig. 21 shows the detail of one of the vortices produced by the Kelvin-Helmholtz instability, computed at $t = 100$ s with different values of C_T. It is observed that solution provided by the TENO method resembles that of the WENO method for a high value of C_T and that of the linear reconstruction for a low value of C_T. The TENO reconstruction is the best choice in this case among the methods examined. It provides the best compromise between accuracy and robustness.

4.8. Case 8. 3D colliding thermals

This test case represents the 3D version of Case 6, as proposed by Norman [42]. It is used to show that the proposed methods can be extended to 3D problems. The problem is defined inside the domain $[0, 20000] \times [0, 20000] \times [0, 10000]$ m^3. To drive the motion, we add a perturbation in the potential temperature

$$\Delta\theta = 20(\max(1 - d_1, 0) + \min(d_2 - 1, 0)); \tag{76}$$

with

$$d_1 = \frac{\sqrt{(x - x_1)^2 + (y - y_1)^2 + (z - z_1)^2}}{r}, \quad d_2 = \frac{\sqrt{(x - x_2)^2 + (y - y_2)^2 + (z - z_2)^2}}{r}, \tag{77}$$

where $r = 2000$ m is the radius of the bubbles, $(x_1, y_1, z_1) = (10000, 10000, 2000)$ m is the center of the warm bubble and $(x_2, y_2, z_2) = (10000, 10000, 8000)$ m is the center of the cold bubble. Fig. 22 shows the iso-surfaces of potential temperature and the velocity field in half-domain at $t = 200$ s, computed by the TENO scheme. The numerical model is able to adequately capture the dynamics of the bubbles.

5. Conclusions

In this work, we present the methodology to construct a family of very high order well-balanced schemes for the computation of the Euler equations with gravitational source term, with application to meso- and micro-scale atmospheric

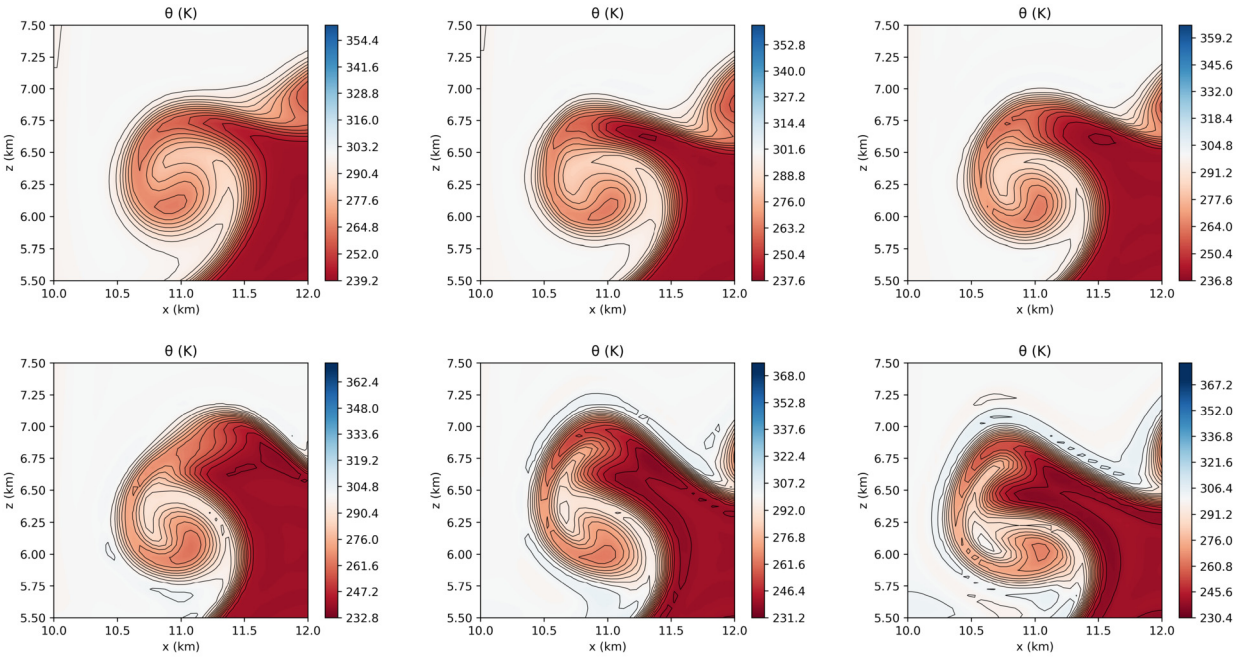

Fig. 21. Case 7. Detail of one of the vortices produced by the Kelvin-Helmholtz instability, computed by the WENO-JS (left-top), TENO ($C_T = 10^{-3}$) (middle-top), TENO ($C_T = 10^{-4}$) (right-top), TENO ($C_T = 10^{-6}$) (left-bottom), TENO ($C_T = 10^{-8}$) (middle-bottom) and linear reconstruction (right-bottom).

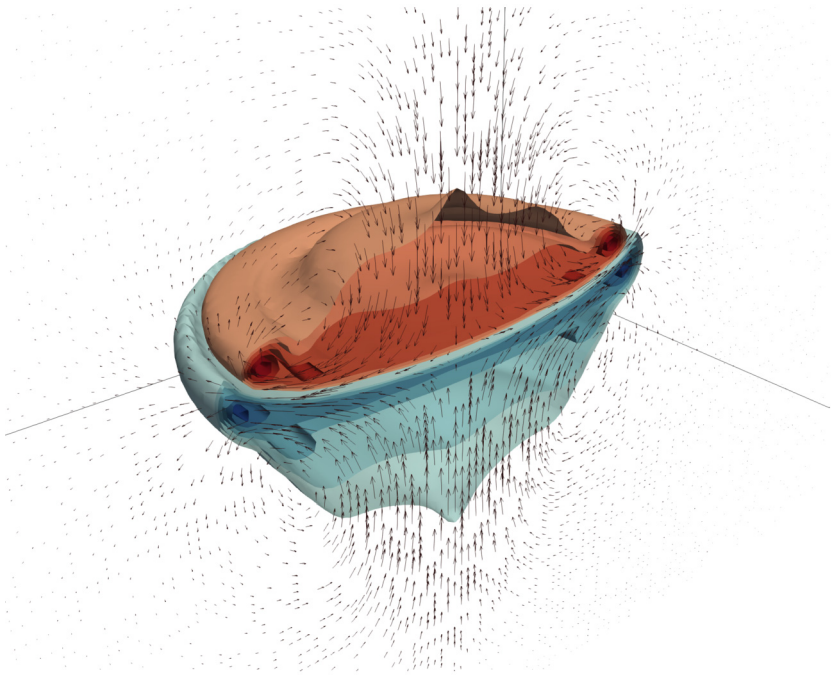

Fig. 22. Case 8. Iso-surfaces of computed potential temperature and velocity field at $t = 200$ s with the TENO scheme.

flows. The proposed method can be combined with essentially non-oscillatory reconstruction schemes (e.g. WENO and TENO), which retain a high order of accuracy in smooth regions and allow computing sharp gradients of the solution without spurious oscillations. The keystone of the method is the use of augmented Riemann solvers to preserve the exact equilibrium between fluxes and source terms at cell interfaces. In particular, we use the HLLS solver, which is applied here for the first time to the Euler equations under gravitation. The numerical results evidence that the proposed approach satisfies the well-balanced property with and without horizontal winds, in 1D, 2D and 3D.

The TENO method has been used as the preferred reconstruction scheme; the WENO and linear reconstructions have also been considered for comparison. To the knowledge of the authors, the TENO method has not been applied to NWP before. Therefore, a thorough assessment of this method is carried out in this work. As expected, the TENO method provides more accurate results at the cost of a higher computational expense. When considering the scenarios involving the propagation of inertia and gravity waves (Cases 2, 3 and 4), the improvement in accuracy is subtle and the WENO reconstruction may be sufficient. On the other hand, when considering slow convective processes with strong shear, numerical dissipation is more visible. In such cases, the TENO reconstruction outperforms the WENO reconstruction, providing a similar accuracy than the linear reconstruction in smooth regions with an enhanced robustness (Cases 5, 6, 7 and 8). This improvement is clearly observed in presence of turbulence (Case 7), where the WENO reconstruction adds an excessive numerical diffusion, damping the small-scale eddies and the linear reconstruction is highly oscillatory. It is worth noting that although the WENO and TENO methods are essentially non-oscillatory, there are some situations where an unphysical overshooting of the potential temperature has been observed. We have shown that a suitable choice of C_T for the TENO reconstruction normally allows damping the spurious oscillations. This issue was already reported in previous works for different numerical schemes, including the WENO scheme [49], and should be further investigated in the future.

The proposed approach can be combined with other augmented Riemann solvers and reconstruction methods. In the future, contact wave-restoring solvers should be considered. Furthermore, the integration in time can be improved using higher order or semi-implicit integration methods [17]. Also note that, for the system considered here, it would be possible to rewrite the proposed scheme in terms of perturbation variables (i.e. by substracting the hydrostatic state). In this case, traditional Riemann solvers could be used and the WENO and TENO reconstructions would be applied similarly.

It must be noted that the proposed schemes enable the simulation of meso- and micro-scale atmospheric flows in an implicit LES (iLES) manner, since the numerical diffusion introduced by the spatial reconstruction and the Riemann solver may play the role of a sub-grid model accounting for the physical dissipation in the unresolved motion [48,65]. The evaluation of the spectral properties of the methods (i.e. combination of Riemann solver and reconstruction scheme) for the resolution of under-resolved turbulent flows should be examined in the future to determine the capabilities of the methods for iLES and cloud resolving purposes. There are previous studies assessing the spectral properties of WENO and TENO methods in combination with different Riemann solvers which can serve as a guideline [26,53,54].

CRediT authorship contribution statement

Adrián Navas-Montilla: Conceptualization, Methodology, Investigation, Formal analysis, Validation, Software, Writing, Funding acquisition. **Isabel Echeverribar:** Investigation, Formal analysis, Validation, Software, Writing.

Declaration of competing interest

The authors declare that they have no known competing financial interests or personal relationships that could have appeared to influence the work reported in this paper.

Data availability

Data will be made available on request.

Acknowledgements

This work was funded by the Fundación Universitaria Antonio Gargallo under the project 2021/B010 (Navas-Montilla). This work has also been partially funded by Gobierno de Aragón through Fondo Social Europeo (T32-20R, Feder 2019-2021 “Construyendo Europa desde Aragón”).

References

[1] F. Acker, R.B. de R. Borges, Bruno Costa, An improved WENO-Z scheme, J. Comput. Phys. 313 (2016) 726–753.
[2] Marc Andrés-Carcasona, M. Soria, E. García-Melendo, A. Miró, Toward a quantitative understanding of Robert’s rising thermal bubble as a benchmark for 3D atmospheric codes, Mon. Weather Rev. 151 (2) (2023) 509–522.
[3] Alfredo Bermudez, Ma Elena Vazquez, Upwind methods for hyperbolic conservation laws with source terms, Comput. Fluids 23 (8) (1994) 1049–1071.
[4] N. Botta, R. Klein, S. Langenberg, S. Lützenkirchen, Well balanced finite volume methods for nearly hydrostatic flows, J. Comput. Phys. 196 (2) (2004) 539–565.
[5] Mark H. Carpenter, Travis C. Fisher, Eric J. Nielsen, Steven H. Frankel, Entropy stable spectral collocation schemes for the Navier–Stokes equations: discontinuous interfaces, SIAM J. Sci. Comput. 36 (5) (2014) B835–B867.
[6] Cristóbal E. Castro, Eleuterio F. Toro, Martin Käser, ADER scheme on unstructured meshes for shallow water: simulation of tsunami waves, Geophys. J. Int. 189 (3) (2012) 1505–1520.
[7] Manuel J. Castro, T. Morales de Luna, Carlos Parés, Well-balanced schemes and path-conservative numerical methods, in: Handbook of Numerical Analysis, vol. 18, Elsevier, 2017, pp. 131–175.
[8] Praveen Chandrashekar, Christian Klingenberg, A second order well-balanced finite volume scheme for Euler equations with gravity, SIAM J. Sci. Comput. 37 (3) (2015) B382–B402.

[9] Alina Chertock, Shumo Cui, Alexander Kurganov, Şeyma Nur Özcan, Eitan Tadmor, Well-balanced schemes for the Euler equations with gravitation: conservative formulation using global fluxes, J. Comput. Phys. 358 (2018) 36–52.
[10] Alina Chertock, Alexander Kurganov, Tong Wu, Jun Yan, Well-balanced numerical method for atmospheric flow equations with gravity, Appl. Math. Comput. 439 (2023) 127587.
[11] Richard Courant, Kurt Friedrichs, Hans Lewy, On the partial difference equations of mathematical physics, IBM J. Res. Dev. 11 (2) (1967) 215–234.
[12] Lin Fu, A very-high-order TENO scheme for all-speed gas dynamics and turbulence, Comput. Phys. Commun. 244 (2019) 117–131.
[13] Lin Fu, Review of the high-order TENO schemes for compressible gas dynamics and turbulence, Arch. Comput. Methods Eng. (2023) 1–34.
[14] Lin Fu, Xiangyu Y. Hu, Nikolaus A. Adams, A family of high-order targeted ENO schemes for compressible-fluid simulations, J. Comput. Phys. 305 (2016) 333–359.
[15] Pilar Garcia-Navarro, Maria Elena Vazquez-Cendon, On numerical treatment of the source terms in the shallow water equations, Comput. Fluids 29 (8) (2000) 951–979.
[16] Debojyoti Ghosh, James D. Baeder, Compact reconstruction schemes with weighted ENO limiting for hyperbolic conservation laws, SIAM J. Sci. Comput. 34 (3) (2012) A1678–A1706.
[17] Debojyoti Ghosh, Emil M. Constantinescu, Semi-implicit time integration of atmospheric flows with characteristic-based flux partitioning, SIAM J. Sci. Comput. 38 (3) (2016) A1848–A1875.
[18] Debojyoti Ghosh, Emil M. Constantinescu, Well-balanced, conservative finite difference algorithm for atmospheric flows, AIAA J. 54 (4) (2016) 1370–1385.
[19] Francis X. Giraldo, Marco Restelli, A study of spectral element and discontinuous Galerkin methods for the Navier–Stokes equations in nonhydrostatic mesoscale atmospheric modeling: equation sets and test cases, J. Comput. Phys. 227 (8) (2008) 3849–3877.
[20] Edwige Godlewski, Pierre-Arnaud Raviart, Numerical Approximation of Hyperbolic Systems of Conservation Laws, vol. 118, Springer Science & Business Media, 2013.
[21] Irene Gómez-Bueno, Manuel J. Castro, Carlos Parés, High-order well-balanced methods for systems of balance laws: a control-based approach, Appl. Math. Comput. 394 (2021) 125820.
[22] Joshua M. Greenberg, Alain-Yves LeRoux, A well-balanced scheme for the numerical processing of source terms in hyperbolic equations, SIAM J. Numer. Anal. 33 (1) (1996) 1–16.
[23] J.E. Guerra, P.A. Ullrich, A high-order staggered finite-element vertical discretization for non-hydrostatic atmospheric models, Geosci. Model Dev. 9 (5) (2016) 2007–2029.
[24] Andrew K. Henrick, Tariq D. Aslam, Joseph M. Powers, Mapped weighted essentially non-oscillatory schemes: achieving optimal order near critical points, J. Comput. Phys. 207 (2) (2005) 542–567.
[25] Zhe Ji, Tian Liang, Lin Fu, A class of new high-order finite-volume TENO schemes for hyperbolic conservation laws with unstructured meshes, J. Sci. Comput. 92 (2) (2022) 1–39.
[26] Feilin Jia, Zhen Gao, Wai Sun Don, A spectral study on the dissipation and dispersion of the WENO schemes, J. Sci. Comput. 63 (1) (2015) 49–77.
[27] Guang-Shan Jiang, Chi-Wang Shu, Efficient implementation of weighted ENO schemes, J. Comput. Phys. 126 (1) (1996) 202–228.
[28] Roger Käppeli, Siddhartha Mishra, Well-balanced schemes for the Euler equations with gravitation, J. Comput. Phys. 259 (2014) 199–219.
[29] Randall J. LeVeque, Balancing source terms and flux gradients in high-resolution Godunov methods: the quasi-steady wave-propagation algorithm, J. Comput. Phys. 146 (1) (1998) 346–365.
[30] Cheng Li, Xi Chen, Simulating nonhydrostatic atmospheres on planets (snap): formulation, validation, and application to the Jovian atmosphere, Astrophys. J. Suppl. Ser. 240 (2) (2019) 37.
[31] Peng Li, Zhen Gao, Simple high order well-balanced finite difference WENO schemes for the Euler equations under gravitational fields, J. Comput. Phys. 437 (2021) 110341.
[32] Simone Marras, James F. Kelly, Margarida Moragues, Andreas Mueller, Michal A. Kopera, Mariano Vazquez, Francis X. Giraldo, Guillaume Houzeaux, Oriol Jorba, A review of element-based Galerkin methods for numerical weather prediction, 2015.
[33] Simone Marras, Margarida Moragues, Mariano Vázquez, Oriol Jorba, Guillaume Houzeaux, A variational multiscale stabilized finite element method for the solution of the Euler equations of nonhydrostatic stratified flows, J. Comput. Phys. 236 (2013) 380–407.
[34] Domingo Muñoz-Esparza, Jeremy A. Sauer, Anders A. Jensen, Lulin Xue, Wojciech W. Grabowski, The fasteddy® resident-GPU accelerated large-eddy simulation framework: moist dynamics extension, validation and sensitivities of modeling non-precipitating shallow cumulus clouds, J. Adv. Model. Earth Syst. 14 (4) (2022) e2021MS002904.
[35] J. Murillo, A. Navas-Montilla, A comprehensive explanation and exercise of the source terms in hyperbolic systems using Roe type solutions. Application to the 1D-2D shallow water equations, Adv. Water Resour. 98 (2016) 70–96.
[36] J. Murillo, A. Navas-Montilla, Pilar García-Navarro, Formulation of exactly balanced solvers for blood flow in elastic vessels and their application to collapsed states, Comput. Fluids 186 (2019) 74–98.
[37] Javier Murillo, P. García-Navarro, Augmented versions of the HLL and HLLC Riemann solvers including source terms in one and two dimensions for shallow flow applications, J. Comput. Phys. 231 (20) (2012) 6861–6906.
[38] Andreas Müller, Jörn Behrens, Francis X. Giraldo, Volkmar Wirth, Comparison between adaptive and uniform discontinuous Galerkin simulations in dry 2D bubble experiments, J. Comput. Phys. 235 (2013) 371–393.
[39] Adrián Navas-Montilla, Carmelo Juez, Mário J. Franca, Javier Murillo, Depth-averaged unsteady RANS simulation of resonant shallow flows in lateral cavities using augmented WENO-ADER schemes, J. Comput. Phys. 395 (2019) 511–536.
[40] Adrián Navas-Montilla, Javier Murillo, Asymptotically and exactly energy balanced augmented flux-ADER schemes with application to hyperbolic conservation laws with geometric source terms, J. Comput. Phys. 317 (2016) 108–147.
[41] Farshid Nazari, Ramachandran D. Nair, A Godunov-type finite-volume solver for nonhydrostatic Euler equations with a time-splitting approach, J. Adv. Model. Earth Syst. 9 (1) (2017) 465–481.
[42] Matthew R. Norman, A high-order WENO-limited finite-volume algorithm for atmospheric flow using the ADER-differential transform time discretization, Q. J. R. Meteorol. Soc. 147 (736) (2021) 1661–1690.
[43] Matthew R. Norman, Ramachandran D. Nair, A positive-definite, WENO-limited, high-order finite volume solver for 2-d transport on the cubed sphere using an ADER time discretization, J. Adv. Model. Earth Syst. 10 (7) (2018) 1587–1612.
[44] Kyle G. Pressel, Colleen M. Kaul, Tapio Schneider, Zhihong Tan, Siddhartha Mishra, Large-eddy simulation in an anelastic framework with closed water and entropy balances, J. Adv. Model. Earth Syst. 7 (3) (2015) 1425–1456.
[45] Kyle G. Pressel, Siddhartha Mishra, Tapio Schneider, Colleen M. Kaul, Zhihong Tan, Numerics and subgrid-scale modeling in large eddy simulations of stratocumulus clouds, J. Adv. Model. Earth Syst. 9 (2) (2017) 1342–1365.
[46] Janusz A. Pudykiewicz, Colm Clancy, Convection experiments with the exponential time integration scheme, J. Comput. Phys. 449 (2022) 110803.
[47] André Robert, Bubble convection experiments with a semi-implicit formulation of the Euler equations, J. Atmos. Sci. 50 (13) (1993) 1865–1873.
[48] Omer San, Kursat Kara, Evaluation of Riemann flux solvers for WENO reconstruction schemes: Kelvin–Helmholtz instability, Comput. Fluids 117 (2015) 24–41.
[49] Julien Savre, James Percival, Michael Herzog, Chris Pain, Two-dimensional evaluation of ATHAM-fluidity, a nonhydrostatic atmospheric model using mixed continuous/discontinuous finite elements and anisotropic grid optimization, Mon. Weather Rev. 144 (11) (2016) 4349–4372.

[50] Chi-Wang Shu, High order weighted essentially nonoscillatory schemes for convection dominated problems, SIAM Rev. 51 (1) (2009) 82–126.
[51] Chi-Wang Shu, Essentially non-oscillatory and weighted essentially non-oscillatory schemes, Acta Numer. 29 (2020) 701–762.
[52] William C. Skamarock, Joseph B. Klemp, Efficiency and accuracy of the Klemp-Wilhelmson time-splitting technique, Mon. Weather Rev. 122 (11) (1994) 2623–2630.
[53] P. Solán-Fustero, Adrián Navas-Montilla, Esteban Ferrer, Juan Manzanero, P. García-Navarro, Application of approximate dispersion-diffusion analyses to under-resolved Burgers turbulence using high resolution WENO and UWC schemes, J. Comput. Phys. 435 (2021) 110246.
[54] Raynold Tan, Andrew Ooi, Two dimensional analysis and optimization of hybrid MDCD-TENO schemes, J. Sci. Comput. 90 (1) (2022) 1–33.
[55] Eleuterio F. Toro, Riemann Solvers and Numerical Methods for Fluid Dynamics: A Practical Introduction, Springer Science & Business Media, 2013.
[56] Panagiotis Tsoutsanis, Antonios Foivos Antoniadis, Dimitris Drikakis, Weno schemes on arbitrary unstructured meshes for laminar, transitional and turbulent flows, J. Comput. Phys. 256 (2014) 254–276.
[57] Panagiotis Tsoutsanis, Dimitris Drikakis, Addressing the challenges of implementation of high-order finite-volume schemes for atmospheric dynamics on unstructured meshes, 2016.
[58] Bart S. van Lith, Jan H.M. ten Thije Boonkkamp, Wilbert L. IJzerman, Embedded WENO: a design strategy to improve existing WENO schemes, J. Comput. Phys. 330 (2017) 529–549.
[59] U.S. Vevek, Bin Zang, Tze How New, Adaptive mapping for high order WENO methods, J. Comput. Phys. 381 (2019) 162–188.
[60] Nils P. Wedi, Karim Yessad, Agathe Untch, The Nonhydrostatic Global IFS/ARPEGE: Model Formulation and Testing, ECMWF, Reading, UK, 2009.
[61] Jan Weinkaemmerer, Ivan Bašták Ďurán, Stephanie Westerhuis, Jürg Schmidli, Stratus over rolling terrain: large-eddy simulation reference and sensitivity to grid spacing and numerics, Q. J. R. Meteorol. Soc. 148 (749) (2022) 3528–3539.
[62] Yulong Xing, Chi-Wang Shu, High order well-balanced WENO scheme for the gas dynamics equations under gravitational fields, J. Sci. Comput. 54 (2) (2013) 645–662.
[63] Yulong Xing, Chi-Wang Shu, Sebastian Noelle, On the advantage of well-balanced schemes for moving-water equilibria of the shallow water equations, J. Sci. Comput. 48 (1) (2011) 339–349.
[64] Xin Zhang, Chao Yan, Feng Qu, An efficient smoothness indicator mapped WENO scheme for hyperbolic conservation laws, Comput. Fluids 240 (2022) 105421.
[65] S. Zhao, N. Lardjane, I. Fedioun, Comparison of improved finite-difference WENO schemes for the implicit large eddy simulation of turbulent non-reacting and reacting high-speed shear flows, Comput. Fluids 95 (2014) 74–87.